MACHINE LEARNING BASED PREDICTIVE MODELING OF STOCHASTIC SYSTEMS

A DISSERTATION
IN
Mechanical Engineering
and
Mathematics

Presented to the Faculty of the University
of Missouri–Kansas City in partial fulfillment of
the requirements for the degree

DOCTOR OF PHILOSOPHY

by
MOHAN KUMAR GAJENDRAN

M.Sc., University of Missouri-Kansas City, MO, USA, 2019

Kansas City, Missouri
2023

MACHINE LEARNING BASED PREDICTIVE MODELING OF STOCHASTIC SYSTEMS

Mohan Kumar Gajendran, Candidate for the DOCTOR OF PHILOSOPHY Degree

University of Missouri–Kansas City, 2023

ABSTRACT

Complex signals are ubiquitous in our daily lives, and interpreting and modeling them is vital for scientific advancement. Traditional methods for predictive modeling of complex signals include statistical signal processing and physics-based simulations. However, statistical signal processing methods often struggle to fully utilize complex and rich datasets, while physics-based simulations can be computationally demanding. As an alternative approach, machine learning (ML) offers a more effective method for the predictive modeling of complex signals.

This research explores the applicability of ML-based predictive modeling to a biomedical and a mechanical system through two case studies. The first case study focuses on developing a machine learning-based model for early-stage glaucoma detection using electroretinogram signals, which has been a challenging problem in ophthalmology. By leveraging medically relevant information contained in ERG signals, the study aims to

establish a novel and reliable predictive framework for the early detection of glaucoma using a machine-learning-based algorithm. The results demonstrate that machine-learning-based models, trained using advanced wavelet-based features, can effectively detect the early stage of glaucoma from ERG stochastic signals.

The second case study centers on developing a machine learning-based model for stall delay correction in wind turbines. Existing stall delay correction models rely on 2D airfoil characteristics, which can lead to inaccuracies in predicting aerodynamic loads during design and, consequently, result in structural failure due to excessive load. To address this issue, the study proposes a novel stall delay correction model based on the soft computing technique of symbolic regression. The model offers high-level precise aerodynamic performance prediction through the blade element momentum process, making it a promising alternative for accurate and efficient stall delay correction in wind turbines.

APPROVAL PAGE

The faculty listed below, appointed by the Dean of the School of Graduate Studies, have examined a dissertation titled "Machine Learning based Predictive Modeling of Stochastic Systems," presented by Mohan Kumar Gajendran, candidate for the Interdisciplinary Ph.D. in Mechanical Engineering and Mathematics degree, and hereby certify that in their opinion it is worthy of acceptance.

Supervisory Committee

Amirfarhang Mehdizadeh, Dr. Ing., Committee Chair
Department of Civil & Mechanical Engineering, UMKC

Majid Bani-Yaghoub, Ph.D.
Department of Mathematics and Statistics

Jerry Richardson, Ph.D.
Department of Civil & Mechanical Engineering, UMKC

Ceki Halmen, Ph.D.
Department of Civil & Mechanical Engineering, UMKC

Fengpeng Sun, Ph.D.
Department of Earth & Environmental Sciences, UMKC

CONTENTS

List of Figures

List of Tables

ACKNOWLEDGEMENTS

I would like to take this opportunity to express my deepest gratitude and appreciation to everyone who has contributed to the successful completion of this thesis. First and foremost, I would like to express my heartfelt thanks to my supervisor, Dr. Amirfarhang Mehdizadeh, for his unwavering support, guidance, and mentorship throughout the entirety of my research process. His expertise in the field and dedication to this project have been invaluable in shaping my research and allowing it to reach fulfillment.

I would also like to extend my deepest gratitude to Dr. Peter Koulen and Vision Research Center, UMKC, for their unwavering support and contributions to this research project. The access to the rich dataset and the funding provided by them were critical to the success of this research, and without their assistance, this project would not have been possible. Furthermore, I want to acknowledge the invaluable support and assistance provided by Dr. Christa Lynn Montgomery in collecting, processing, and analyzing the data. Her contributions have been instrumental in the success of this research, and I am truly grateful for the time and effort she invested in this project.

I would like to express my deepest appreciation to Dr. Ijaz Fazil for their invaluable contributions to this research project. Their expertise in the field of wind turbine technology and the access to rich data provided were crucial for the successful completion of this study. Dr. Ijaz Fazil's guidance and support throughout the research process helped me to navigate the complexities of the subject and allowed me to achieve a deeper understanding of the field.

Additionally, I would like to thank the other members of my thesis committee, Dr. Majid Bani-Yaghoub, Dr. Jerry Richardson, Dr. Ceki Halmen, and Dr. Fengpeng Sun for their valuable insights, comments, and feedback throughout the research journey. Their guidance and support have been crucial to my growth as a researcher, and I am truly grateful for the time and effort that they invested in me and my work.

Finally, I would like to thank my family and friends for their unwavering support and encouragement throughout the research process. Their love and support have been a constant source of inspiration, and I could not have completed this thesis without them.

CHAPTER 1

INTRODUCTION

1.1 Background

1.1.1 Introduction to Stochastic systems

Stochastic systems are characterized by their behavior, which is determined by random processes or variables. These variables can be continuous or discrete, and probability distributions describe the system's evolution. Stochastic systems are often employed to model complex systems that exhibit randomness or uncertainty in various fields, such as medicine, engineering, finance, physics, and chemistry.

In medicine, stochastic systems model diverse phenomena, including disease spread, treatment effectiveness, and chronic illness progression. They play a significant role in medical imaging and biomedical signal processing, as well as medical decision support systems. With the increasing availability of large amounts of medical data and advancements in computational methods, machine learning and predictive modeling techniques have gained interest in analyzing data and supporting medical decision-making. These techniques, along with stochastic models, have the potential to improve the diagnosis and treatment of numerous medical conditions.

In engineering, stochastic systems are employed to model phenomena in mechanical systems, structures, and materials. They are widely used in mechanical engineering to understand systems under uncertainty and design robust and reliable systems that operate

under these conditions. Additionally, they can enhance system performance and efficiency through optimization techniques.

In finance, stochastic models describe the behavior of stock prices, interest rates, and other financial variables. In physics, they model systems at the molecular or subatomic level, and in chemistry, they describe chemical reactions and molecular system dynamics.

Stochastic systems often exhibit complex and nonlinear behavior, making them difficult to predict. Consequently, there has been extensive research on developing mathematical models and computational methods for analyzing and understanding these systems' behavior.

1.1.2 Introduction to Machine Learning

Machine learning, a subfield of artificial intelligence, involves developing algorithms and statistical models that learn from data and make predictions or decisions without explicit programming. The goal is to create systems that automatically improve their performance with experience. Machine learning types include supervised learning, unsupervised learning, and reinforcement learning.

Machine learning has gained increasing interest for the understanding and predictive modeling of stochastic systems. It provides powerful tools for analysis and prediction, even for complex or non-linear systems. These techniques can analyze large amounts of data and extract patterns for predictions. In this research, a machine learning algorithm will be employed to analyze and predict stochastic system behavior, aiming to enhance the understanding and predictive modeling of such systems.

1.1.3 Challenges in Predictive Modeling of Stochastic Systems

Predictive modeling of stochastic systems faces several challenges, including:

- Modeling Complexity: Stochastic systems can be highly complex, with many interacting components and nonlinear behavior, making it challenging to develop accurate models that capture the system's behavior.
- Lack of Data: Predictive modeling often relies on extensive data, but obtaining high-quality data for stochastic systems may be difficult if the system is challenging to measure or if data collection is expensive.
- Handling high-dimensional systems: Many stochastic systems have numerous variables, complicating the modeling and analysis process.

1.1.4 Importance of Machine Learning in Predictive Modeling of Stochastic Systems

The importance of machine learning in the predictive modeling of stochastic systems lies in its ability to learn from data and make predictions without explicit programming. Machine learning algorithms can handle large amounts of data, model uncertainty, learn complex nonlinear relationships, identify essential variables and patterns, and improve prediction accuracy.

Machine learning's key advantages for predictive modeling include its ability to process large amounts of data and handle uncertainty. Stochastic systems are characterized by uncertainty, complicating accurate predictions. Machine learning algorithms can model and reason with uncertainty, making predictions even in the presence of incomplete or

noisy data. Furthermore, machine learning can learn from nonlinear relationships, identify important features or variables that significantly impact the system's behavior, and detect crucial patterns or structures in the data. This information can be valuable for understanding the stochastic system's underlying mechanisms and enhancing its predictive modeling.

Traditional methods, such as linear regression and Gaussian processes, may not accurately model non-linear systems. However, machine learning techniques like neural networks and non-parametric regression can learn complex non-linear relationships and make predictions accordingly. By identifying essential features or variables, machine learning can help determine the factors that most influence the system's behavior, enabling a deeper understanding of the system. Additionally, machine learning can identify crucial patterns or structures in the data, which can be employed to recognize important states or regions of the system's behavior.

1.2 Case Study 1: ML-based predictive modeling of a biomedical system

1.2.1 Background

In recent years, machine learning (ML) has emerged as a powerful tool for analyzing and modeling complex biomedical systems. ML-based methods have been successfully applied to a wide range of medical applications, including disease diagnosis, risk prediction, and treatment optimization. One such application is the early detection of glaucoma using electroretinogram (ERG) signals. Glaucoma, a leading cause of irreversible blindness, can be effectively managed if detected early. However, conventional diagnostic methods often fail to identify the disease in its initial stages, necessitating the development of more

sophisticated techniques.

1.2.2 Motivation

The application of ML-based predictive modeling in biomedical systems has the potential to revolutionize the field of medicine by enabling more accurate and personalized care. By investigating the effectiveness of ML methods in predicting and diagnosing complex diseases, such as glaucoma, using ERG signals, this research seeks to contribute to the growing body of knowledge in this domain and improve early detection of the disease.

1.2.3 Current State of the Art and Research Gaps

While ML has been successfully applied in various biomedical applications, there are still limitations and gaps that need to be addressed. In particular, the identification of appropriate features, selection of optimal ML algorithms, and validation of the predictive models remain challenges. Additionally, the translation of ML-based methods from one species to another requires further investigation.

1.2.4 Problem Statement

The present study aims to explore the feasibility of applying ML-based methods to the analysis of ERG signals for detecting glaucoma at different stages of the disease. The study will focus on determining the most effective features and algorithms for achieving accurate and reliable predictions.

1.2.5 Research Objectives

The objectives of this study are as follows:

1. To systematically apply ML-based methods to identify the most informative features and ML algorithms for accurate glaucoma detection and disease progression prediction.

2. To systematically apply ML-based methods to predict retinal ganglion cell (RGC) loss based on ERG signals.

1.2.6 Summary of Contributions

This research will contribute to the field of ML-based predictive modeling in biomedical systems by developing a novel approach to glaucoma detection and disease progression prediction based on ERG signals. The study will also identify key features and algorithms for accurate and reliable predictions, as well as provide insights into the potential application of ML methods in other areas of medicine.

1.2.7 Significance of Study

The successful implementation of ML-based methods for early detection of glaucoma using ERG signals has the potential to significantly impact the field of ophthalmology. Improved early detection can lead to better management of the disease, ultimately reducing the incidence of irreversible blindness. Additionally, the findings of this study may contribute to the development of new diagnostic tools and methodologies that can be applied to other diseases and medical conditions.

1.3 Case Study 2: ML-based predictive modeling of a mechanical system

1.3.1 Background

In recent years, machine learning (ML) techniques have gained significant traction in various fields of engineering, including the modeling and prediction of mechanical systems. The application of ML techniques to mechanical systems, such as wind turbines, offers an opportunity to enhance the accuracy and efficiency of predictive models, particularly for complex phenomena like stall delay correction. Traditional methods for stall delay correction in wind turbine performance prediction, such as Blade Element Momentum (BEM) analysis, often struggle to provide accurate results due to the inherent complexities and uncertainties in the aerodynamic loads experienced by the rotor blades.

1.3.2 Motivation

The motivation for this study lies in the need for more accurate and efficient predictive models for stall delay correction in wind turbine performance prediction. Improved models can help to prevent structural failure and excessive loading on wind turbine blades, which can lead to more reliable and efficient wind energy systems. By employing ML-based techniques, this study aims to address the limitations of traditional methods and contribute to the development of enhanced predictive models for mechanical systems like wind turbines.

1.3.3 Current State of the Art and Research Gaps

Although there has been progress in developing correction models for stall delay using conventional hard computing techniques, these models have been found to be inadequate in accurately predicting the enhancement in lift coefficients due to stall delay. Recent research has started to explore the potential of ML-based techniques for improving the accuracy of these models. However, there remains a gap in the literature regarding the development and validation of ML-based predictive models specifically for stall delay correction in wind turbine performance prediction.

1.3.4 Problem Statement

The problem to be addressed in this study is the development and validation of an ML-based predictive model for stall delay correction in wind turbine performance prediction, focusing on accurately capturing the complex aerodynamic phenomena experienced by rotor blades during stall delay conditions.

1.3.5 Research Objectives

The objectives of this study are as follows:

1. To review and analyze the existing approaches for stall delay correction in wind turbine performance prediction.

2. To develop a machine learning-based predictive model that accurately captures the stall delay phenomenon in wind turbine rotor blades.

3. To validate the proposed ML-based model using experimental and computational

data from wind turbine performance studies, such as the NREL Phase VI turbine and MEXICO rotor.

4. To identify the limitations and research gaps in the current state-of-the-art models and address these limitations using the proposed ML-based model.

1.3.6 Summary of Contributions

The main contributions of this study include:

1. The development of an ML-based predictive model for stall delay correction in wind turbine performance prediction.

2. The validation of the proposed model using published data from wind turbines demonstrating improved accuracy and efficiency compared to existing models.

3. The identification of potential areas for future research and development in ML-based modeling of mechanical systems, particularly in the context of wind energy systems.

1.3.7 Significance of Study

The significance of this study lies in its potential to improve the accuracy and efficiency of stall delay correction models in wind turbine performance prediction. By addressing the limitations of traditional methods and providing a more accurate and efficient alternative, the proposed ML-based model can contribute to the development of more reliable and cost-effective wind energy systems, which are essential for addressing the growing demand for renewable energy sources.

1.4 Outline of Dissertation

This dissertation focuses on machine learning-based predictive modeling of stochastic systems, covering two diverse case studies. The introduction provides an overview of the background and motivation, problem statement, research objectives, summary of contributions, significance of the study, and the outline of the dissertation. The growing need for accurate predictive modeling in stochastic systems is highlighted, emphasizing the potential of machine learning techniques to address complex problems.

The study is divided into two major case studies. The first case study presents a novel machine-learning based framework for detecting early-stage glaucoma using electroretinography data. The introduction, methods, results, and discussion of this case study are covered in detail, illustrating the effectiveness of the proposed framework. The second case study investigates a machine-learning-based stall delay correction model for improving blade element momentum analysis in wind turbine performance prediction. This section includes an introduction, description of the stall delay mechanism, blade element momentum theory, models for stall delay correction, experimental descriptions, symbolic regression, a new empirical model for stall delay, results and discussions, and conclusions and future works.

The dissertation concludes with a summary of the findings and their implications for the broader field of machine learning-based predictive modeling of stochastic systems. The potential of the proposed ML-based models for the early detection of glaucoma and improving stall delay correction in wind turbine performance prediction is discussed, highlighting the benefits of using machine learning techniques to address complex problems

in diverse domains. The reference list and vita are provided at the end of the document.

CHAPTER 2

CASE STUDY 1: NOVEL MACHINE-LEARNING BASED FRAMEWORK USING ELECTRORETINOGRAPHY DATA FOR THE DETECTION OF EARLY-STAGE GLAUCOMA

2.1 Introduction

Glaucoma, a chronic neurodegenerative disease affecting the retina and optic nerve, and a leading cause of blindness, is characterized by a progressive, irreversible loss of vision. As currently available treatment paradigms focus primarily on a predisposing factor, elevated intraocular pressure (IOP), and do not allow for repair of the retina and optic nerve once the disease has progressed and damage has occurred, technologies enabling an early diagnosis of glaucoma are needed urgently. Consequently, such new diagnostic modalities enabling early therapeutic intervention would significantly improve treatment outcomes. Current methods of glaucoma diagnosis are based on psychophysical techniques and the assessment of structural changes to the retina and optic nerve [4]. Standard automated perimetry testing, including the widely used Humphrey visual field testing, currently represents the most commonly utilized technique for glaucoma diagnosis and monitoring of disease progression and therapy outcomes [5, 6]. Recent efforts to employ machine-learning (ML) approaches to improve the analysis of behavioral psychophysical testing approaches produced moderate improvements over conventional analysis algorithms [7]. However, significant damage to the retina and optic nerve, including loss of retinal ganglion cells (RGCs) has often already occurred before changes can be detected with standard

automated perimetry testing [8].

Recently, automated retinal image analysis (ARIA) systems have been developed for the diagnosis of complex diseases such as diabetic retinopathy and glaucoma [9, 10]. The development of these ARIA systems involved ML-based methods to detect structural changes determined with optical coherence tomography (OCT) imaging resulting in high analytical accuracy in automatically classifying disease phenotypes based on structural characteristics [11–13]. Despite such significant progress, early detection of glaucoma is still a challenge [14], given the highly significant limitations of early detection of glaucoma based on structural methods. Systems employing the analysis of structural changes for glaucoma diagnosis are based on measuring retinal nerve fiber layer (RNFL) thickness in OCT images of the retina, which is highly variable and weakly correlated with RGC counts despite RNFL thickness being a surrogate marker of RGC degeneration and optic nerve fiber loss, hallmarks of glaucoma pathogenesis [15]. Further, RGC loss often occurs early during pathogenesis in the absence of measurable RNFL thinning, prompting an urgent clinical need for methods with higher sensitivity, such as functional measures including ERG [14–18]. In contrast, functional measures such as visual field and ERG are sensitive to subtle changes in RGC function and RGC damage, which suggest a significant potential to enable early detection of glaucoma, even in the absence of elevated IOP, as seen in patients with normotensive glaucoma [14, 17, 19]. Therefore, this study aims to investigate such potential considering ERG signals. Consequently, interventions could be initiated before irreversible damage occurs, allowing for the optimization of treatment strategies based on the improvement of RGC function [20]. This is of high clinical importance as determining

the efficacy of therapies aimed at lowering IOP in open-angle glaucoma [21, 22] requires early validation of therapy success [13], but will also be of importance for the development of novel alternative and complementary glaucoma therapies based on neuroprotective strategies [23]. Recently, in a study conducted by [24] photopic negative response (PhNR) was used to assess the short-term changes in inner retinal function following intraocular pressure (IOP) decrease in glaucoma using eyedrops. [25] showed that Nicotinamide supplementation helps improve the function of the inner retina in glaucoma.

Recent advances in the acquisition of complex neuroscience data have a significant innovative potential to progress towards more effective diagnostic systems [26]. The adequate, timely, and clinically relevant analysis of such data has potentially high clinical impact [27]. However, while such data sets can be readily acquired and technologies to further improve and simplify data acquisition continue to emerge [28], critical barriers to implement the effective use of such novel data in clinical diagnostics and therapy delivery remain [29]. While the analysis of complex biomedical data is often part of medical diagnostics, current expert analysis standards and algorithms are limited by pattern recognition in few dimensions, which results in less than optimal identification or even exclusion of potentially relevant diagnostic features [30]. Machine learning could significantly augment medical diagnostics and increase their efficacy by analyzing aspects of complex and multi-dimensional biomedical data that are either not being considered adequately or that are not accessible to current analysis methods [31]. Such machine-learning based diagnostic approaches have been developed and are being actively used for the detection of cardiovascular diseases [32], and cancer [33].

ERG data are one such type of complex and multi-dimensional biomedical data that are potentially relevant to the diagnosis of glaucoma, but are currently not considered during routine clinical practice or in clinical research. Historically, this is due to multiple barriers related to clinical ERG data acquisition, such as limitations in reproducibility, high costs of both equipment and of individual tests, long test duration and complex test administration resulting in reduced patient acceptance and compliance, and the need for highly trained experts to administer tests. With the advent of novel ERG technologies, most of these barriers related to clinical ERG data acquisition have been removed [34–39], opening up the possibility to effectively use ERG data for glaucoma diagnostics, calling the necessity for the development of novel approaches (e.g., M-L-based ones) that is capable to quickly and thoroughly analyze such data.

Machine learning is based on statistical techniques to learn from data and develop predictive models [40]. Recently, there has been a surge of interest in machine learning as significant advancements in computational hardware [41] facilitate the development of novel machine learning approaches as solutions to problems in various disciplines from financial forecasting to public transportation and healthcare [42–44]. There are several predictive techniques in machine learning with various complexities, ranging from simple linear models to advanced non-linear models such as those based on deep learning algorithms [45–47]. Currently, available ERG analysis methods, such as those developed by Hood, Birch, and Porciatti [20, 48], have contributed to a significantly improved understanding of the relationship between ERG signals and vision loss. These methods are limited to frequency domain analysis [49–52] and the analyses of differences in amplitude

and latency of ERG [53–59]. In addition, these methods are often time-consuming, labor-intensive, and focused on parameters developed to address a small subset of mostly genetic diseases of the eye affecting predominantly pediatric patient populations [60–62]. To achieve higher accuracy and a more detailed understanding of disease progression and of the impact of therapeutic intervention, more sophisticated features such as those obtained from wavelet analysis are required [63, 64]. Additionally, currently available methods are often not suitable for analyzing large data sets and databases, rendering them incapable of taking advantage of complex and rich datasets [65, 66]. These drawbacks prompted others [67–70] and us to design and develop novel methods capable of handling complex and large datasets and ultimately to provide a unique approach for diagnosing early-stage glaucoma. However, it should be noted that early detection of glaucoma is not possible with currently available techniques during the early stages of glaucoma pathogenesis, when cellular changes occur that do not result in structural damage or visual impairment yet. Such early-onset factors predisposing to glaucoma development include processes preceding the onset of ocular hypertension, for example, the onset of iris pigment dispersion preceding IOP elevation in the DBA/2 mouse model. However, and more importantly, we identified cellular changes resulting in altered ERG signals, such as changes in oscillatory potentials, that currently cannot be detected with other functional or structural measures.

Boquete and colleagues developed a method to automate glaucoma diagnosis based on ERG signals using neural networks and structural pattern analysis [71]. They utilized thirteen features (morphological and transitional characteristics) for training the model and achieved a testing accuracy of 80.7% [71]. This study was limited to basic

morphological characteristics of mfERG recordings [71]. Miguel and colleagues [72] also employed neural networks for ERG-based glaucoma diagnosis but used continuous wavelet transformed coefficients and achieved a binary classification accuracy of 86.90% [72]. Although a higher accuracy was achieved, this analysis was limited to wavelet features only [72]. Nevertheless, both studies showed that machine learning-based methods trained even on compact data sets provide powerful tools to analyze ERG signals and provide potentially new information relevant for the early detection of glaucoma. Sarossy and colleagues investigated the relationship between a compact set of features and glaucoma that can be analyzed with machine learning approaches; however, the study was limited to the analysis of the photopic negative response (PhNR) and five additional features [73].

The goal of the present study was to comprehensively assess the capability of machine-learning-based methods to detect early-stage glaucoma using time-series ERG signals. In particular, the following points are addressed during method development:

1. Develop a framework to extract and identify important predictors (features) from ERG signals.

2. Compare the predictive capability of statistical and wavelet-based features for binary and multiclass classification.

3. Develop a robust ML-based model to diagnose glaucoma (binary classification).

4. Develop a robust ML-based model capable of distinguishing various stages of glaucoma progression (multiclass classification).

5. Develop a robust ML-based model to provide a quantitative assessment of visual function by predicting retinal ganglion cell count from ERG signals for the first time.

2.2 Methods

2.2.1 Overview

ML based algorithms have been applied to Electrocardiogram (ECG) signals in order to develop predictive models for diagnosing heart diseases [32,74]. Recently machine learning-based Artificial Neural Networks (ANN) have been applied to ERG signals for obesity diagnosis [75]. However, to date, machine learning-based methods have not been applied systematically to analyze ERG signals for glaucoma detection. Therefore, the potential of ERG signals in glaucoma diagnosis has not been fully utilized. The present work aims to develop a predictive model for early glaucoma diagnosis based on machine-learning algorithms by utilizing advanced features from ERG signals as predictors. The steps involved in developing a machine-learning-based predictive model for ERG analysis are shown in Figure 1. Each of these steps is explained in detail below.

2.2.2 ERG: A Biomarker

Electroretinography measures the electrical responses of different types of cells in the retina, such as ganglion cells. These signals are usually measured in microvolts. Oscillatory Potential (OP) and Scotopic Threshold Response (STR) represent important ERG components indicative of RGC cell function [76–79]. OPs are small rhythmic wavelets superimposed on the ascending b-wave of the ERG and STR are negative corneal deflection elicited in the fully dark-adapted eye to dim stimuli. An International Society for

Figure 1: Machine learning workflow using ERG signals. *ERG Database:* the ERG database contains the input ERG data used to train the predictive model. *Pre-Processing of data:* this step ensures data quality by transforming the data to a common baseline, accounting for missing data, and handling outliers. *Feature extraction:* mathematical operations are performed on the data to extract features/parameters that indicate functional deficits in the eye. *Predictive Model Development:* algorithms can determine trends and patterns in data from statistical analysis of extracted features during training; these models can predict either class or value from the input data are called classifier and regression models, respectively. *Deployment of Model into medical devices:* successful predictive models can be included with ERG testing devices to provide real-time prognosis and diagnosis.

Clinical Electrophysiology of Vision (ISCEV) standardized ERG protocol [80] included several tests to measure the function of various retinal cell types, including the rod response, standard rod-cone response, Hi-intensity rods, and cones response, cone response, Hi-intensity cone response, flicker, and Hi flicker [81]. A visualization of nine ERG signals resulting from two ERG components (OP and STR) and seven ERG test responses is provided in Figure 2. The dynamics of ERG signals vary in people with various conditions and can therefore aid in differentiating individuals with glaucoma [81], schizophrenia [82], obesity [75], and bipolar disorder [83]. ERG can also help in evaluating the effectiveness of new or existing drugs and therapy modalities [84–87].

2.2.3 Ganzfeld Flash Electroretinography

The development of pigmentary glaucomatous optic neuropathy in the DBA/2 mouse model had several similarities to glaucoma pathogenesis in human patients, including loss of vision and RGC [88–94]. The Ganzfeld flash electroretinography (fERG) procedures in mice were conducted under dim red light that was followed by an overnight dark adaptation (>12 h). Isoflurane at 3% and 1.5% was used respectively, to anesthetize mice and maintain anesthesia. The pupils were dilated using 1 drop of 1% tropicamide and were allowed to dilate for 10 minutes. Rectal temperature was monitored and maintained at 37Â°C using a heating pad. Silver-embedded thread electrodes were placed over the cornea in 1% methylcellulose with mini-contact lenses fitted preventing the corneal dehydration (Ocuscience LLC, Henderson, NV). The head was placed inside the Ganzfeld dome, and fERG with 2 recording channels was performed using an HMsERG system (Ocuscience LLC) equipped with an amplifier with a band pass from 0.3 to 300 Hz. Mice were subjected to the International Society for Clinical Electrophysiology of Vision (ISCEV) standardized ERG protocol [29], whose implementation is described in detail in [80]. ERGView 4.380V software (OcuScience LLC) was used to perform statistical analyses including averaging multiple flashes recorded at each intensity and stored for further analysis. Additionally, mice were tested using a scotopic flash intensity series in the range of -4.5 to 1.5 log cd s/m^2. Further, a 1:1000 neutral density filter (ND3) was used to control the 7 lowest flash intensities; data were averaged from 10 flashes (-4.5 to -3.5 log cd s/m^2), 4 flashes (-3 to 0.5 log cd s/m^2) at the lower intensities or measured from 1 flash at the 2 highest intensities (1 to 1.5 log cd s/m^2). Following the light adaptation (1.5 log cd s/m^2 for 10

min), responses from a photopic series (-2 to 1.5 log cd s/m^2; 32 flashes per intensity) were recorded in a separate fashion. Further details about data acquisition can be found in [81].

2.2.4 ERG Dataset

Ganzfeld fERG tests were performed on four months old (n=15) and 11 months old (n=15) male DBA/2 mice. Each animal had two sets of test data, one for each eye. Therefore, a total of 60 data sets for individual eyes were included in this study. Each data set comprised of nine different ERG signals (OP, STR, and seven signals from ERG testing protocols), as shown in Figure 2, (OPs are small rhythmic wavelets superimposed on the ascending b-wave of the ERG and STR are negative corneal deflection elicited in the fully dark-adapted eye to dim stimuli). Therefore, 540 recordings were utilized in this study. Intraocular pressure (IOP) and retinal ganglion cell (RGC) count measurements were also utilized in this study. Although IOP data was available for all animals, RGC counts were only available for ten (twenty eyes). The animals were grouped in a binary group (healthy and glaucomatous) based on age and multiclass group based on IOP as (normal, $<$12 mm Hg; high, [$\geq$12 mm Hg $<$17 mm Hg]; glaucomatous, $\geq$17 mm Hg). All the data used in this study was well balanced for respective groups.

2.2.5 Pre-Processing of Data

ERG raw data may contain several anomalies such as different start times, missing data, different sampling frequencies, noise, and unequal lengths of the signal recordings. In Machine learning-based modeling, the quality of the training data can significantly impact the model performance. Therefore, pre-processing (data preparation and screening)

is crucial to ensure the quality of the training dataset [95]. Pre-processing steps considered in the present study include,

1. Baseline adjustment
2. Feature extraction
3. Handling missing data
4. Handling outliers
5. Feature scaling
6. Feature selection

The signal's baseline (start time) can be different for different animals and testing protocols. Therefore, all the measurements were brought to a common baseline (start time was offset to zero) during baseline adjustment [95]. Feature extraction involves computing a reduced set of values from a high-dimensional signal capable of summarizing most of the information contained in the signal [96]. The missing data were replaced with mean values [97]. For handing outliers, values more than three scaled median absolute deviations (MAD) away from the median were detected as outliers and replaced with threshold values used in outlier detection [98]. The feature's values vary widely, even by orders of magnitude. Therefore, it is important to bring the feature values to a similar range (feature scaling), especially when using distance-based machine learning algorithms [99]. Feature selection is further dimensionality reduction from the extracted features. It is performed to reduce the computational cost of modeling, to achieve a better generalized,

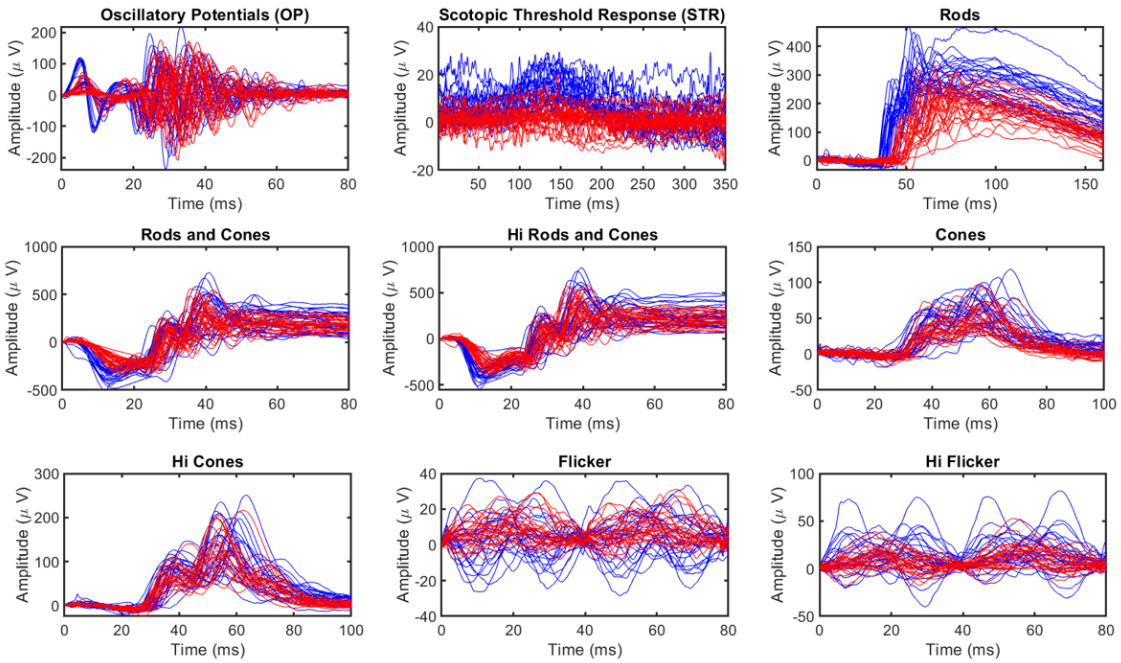

Figure 2: Visualization of ERG Signals manifesting their complex nature. The blue lines correspond to healthy and red lines correspond to glaucomatous Signals. Electroretinogram (ERG) tests are a group of diagnostic procedures that evaluate the functionality of various components of the retina. These tests include **Oscillatory Potential (OP)**, which are small rhythmic wavelets that appear on the ascending b-wave of the ERG; **Scotopic Threshold Response (STR)**, a negative corneal deflection observed in fully dark-adapted eyes when exposed to dim stimuli; **Rod response**, which assesses the activity of rod photoreceptors; **Standard rod-cone response**, which measures the combined activity of both rods and cones; **Hi-intensity rods and cones response**, which evaluates the combined performance of rods and cones under high-intensity light; **Cone response**, which focuses on the function of cone photoreceptors; **Hi-intensity cone response**, which examines cone function under high-intensity light; **Flicker response**, which assesses retinal response to rapid changes in light intensity; and finally, **Hi-intensity flicker response**, which measures the same response under high-intensity light conditions. These various ERG signals provide a comprehensive evaluation of retinal function for diagnostic and research purposes.

high-performance model that is simple and easy to understand [100]. Feature extraction and selection are explained in detail in the following sections.

2.2.6 Feature Extraction

ERG signals are complex high-dimensional data, and training a model with many variables requires significant computational resources. Feature extraction reduces the dimensionality of the data by computing a reduced set of values from a high-dimensional signal capable of summarizing most of the information contained in the signal [101]. In the present study, feature extraction was performed in two phases. First, common statistical features were extracted from the signal, followed by the extraction of advanced wavelet-based features. Figure 3. provides an overview of the feature extraction process and is explained below.

2.2.6.1 Statistical Feature Extraction

A total of 17 Statistical features capable of describing the general behavior of ERG signals were extracted from the signal. These features were grouped as follows.

1. Measures of Central Tendency
2. Measures of Spread
3. Measures of Shape
4. Measures of Peaks
5. Measures of Derivatives

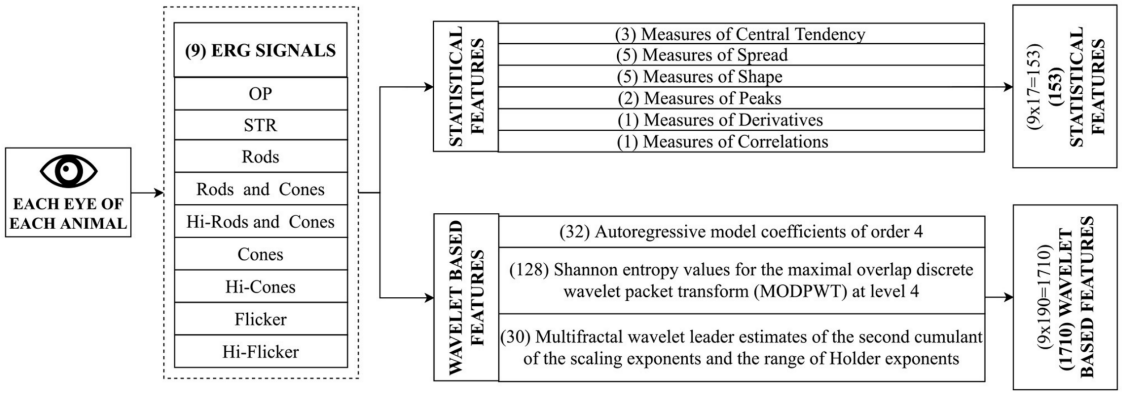

Figure 3: Feature Extraction. During this process, mathematical operations are performed on the data to extract features. This step is crucial for discovering features indicative of functional deficits in the eye. ERG test on each eye leads to nine signals, as shown in Fig. 2. Two sets of features (Standard features and advanced features) are extracted from each of the nine signals. The standard set of features include common statistical features such as mean, quartiles, and entropies. In contrast, the advanced set of features include sophisticated features such as autoregressive coefficients, Shannon entropy, and wavelet features.

6. Measures of Correlation

Measures of central tendency included mean, median, trimmed mean. Measures of spread included range, standard deviation, variance, mean absolute deviation and interquartile range. Measures of the shape include skewness, kurtosis, central moments of the second and third-order, and aspect ratio. Measures of peaks included the number of peaks and troughs in the signal. Measures of derivatives include the first-order derivative of the signal with respect to time. Measures of correlation included the correlation coefficient of the signal with respect to time. The equations for the computation of these quantities can be found in [75, 102].

2.2.6.2 Advanced Feature Extraction

Wavelet-based features and autoregressive analysis serve as advanced statistical measures in the analysis of electroretinogram (ERG) signals, offering valuable insights into the complex patterns and subtle changes within the data. Utilizing wavelet transforms, these features decompose the original signal into multiple levels of detail, providing essential statistical information across various scales. This unique capability enables the analysis of the same signal at different time points, allowing for a comprehensive understanding of the signal's behavior.

Autoregressive analysis complements wavelet-based features by modeling the signal as a linear combination of its previous values, capturing the temporal dependencies and dynamics in the ERG data. This method allows for the efficient representation and analysis of the signal, providing additional information on the structure and patterns within the data.

Advanced features capable of capturing subtle changes were extracted from the signal. Each signal was split into 32 blocks ($\sim$ 2000 samples/block) to further capture subtle changes in the signal [103]. Daubechies least-asymmetric wavelet with four vanishing moments (Symlets 4) was used as mother wavelet to derive the wavelet coefficients [104]. The following features (190 features in total as shown in Figure 3) were extracted from each block of the signal:

AR coefficients: The signal $x[n]$ at time instant n in an AR process of order p can be described as a linear combination of p earlier values of the same signal. The procedure is modeled as follows:

$$x[n] = \sum_{i=1}^{p} a[i]x[n-i] + e[n] \tag{2.1}$$

where $a[i]$ is the AR model's i^{th} coefficient, $e[n]$ denotes white noise with mean zero, and p denotes the AR order. The AR coefficients for each block were estimated using the Burg method [105]; the order was determined using the ARfit model order selection method [106] as 4th order. Therefore a 4-order AR model is chosen to represent each of the ERG signal components.

Wavelet based Shannon Entropy: The Shannon entropy is an information-theoretic measure of a signal. Shannon entropy (denoted as SE) values for the maximal overlap discrete wavelet packet transform (MOD- PWT) using four-level wavelet decomposition was computed on the terminal nodes of the wavelet [107]. Mathematical expression for Shannon entropy using wavelet packet transform is as follows:

$$SE_j = -\sum_{k=1}^{N} p_{j,k} * \log p_{j,k} \tag{2.2}$$

where N is the number of coefficients in the j^{th} node and $p_{j,k}$ are the normalized squares of the wavelet packet coefficients in the j^{th} terminal node of the wavelet.

Multifractal wavelet leader estimates and multiscale wavelet variance estimates: The multifractal measure of the ERG signal was obtained using two wavelet methods (wavelet leader and cumulant of the scaling exponents). Wavelet leaders are time/space-localized suprema of the discrete wavelet coefficients' absolute value. These suprema are used to calculate the Holder exponents, which characterize the local regularity. In addition, second cumulant of the scaling exponents were obtained. Scaling exponents

are scale-dependent exponents that describe the signal's power-law behavior at various resolutions. The second cumulant basically depicts the scaling exponents' divergence from linearity [108]. Wavelet variance of ERG signals were also obtained as features. Wavelet variance quantifies the degree of variability in a signal byÂ scale, or more precisely, the degree of variability in a signal between octave-band frequency intervals [109].

2.2.7 Feature Selection

Feature extraction discussed previously was performed in order to reduce the dimensionality of the signals; however, the resulting number of features was still higher than the number of training data. Therefore, further reduction in the dimensionality of the data was performed using the feature selection method to identify relevant features for classification and regression. It should be noted that feature selection was necessary to reduce the computational cost of modeling, prevent the generation of a complex and over-fitted model with high generalization error, and generate a high-performance model that is simple and easy to understand [110]. In particular, the Minimum Redundancy Maximum Relevance (MRMR) sequential feature selection algorithm was used in the present study because this algorithm is specifically designed to drop redundant features (see [111, 112] for mathematical details/formulations), which was required to design a compact and efficient machine-learning-based model [113]. It is worth noting that other available dimensionality reduction techniques such as Principal component analysis (PCA) were not considered in this study as such techniques do not allow for direct tracing and understanding the relevance of each feature [100].

2.2.8 Predictive Model Development

ML models are mathematical algorithms that provide predictions based on an inference derived from the generalizable predictive patterns of the training data [114]. Several machine learning models were employed and evaluated in order to identify the best one to classify the ERG signals. These included decision trees, discriminant, support vector machine, nearest neighbor, and ensemble classifiers. Most of these models can perform both classification and regression. Decision tree-based models predict the target variable by learning simple decision rules [115]. Discriminant classifiers are based on the assumption that each class has different Gaussian distributions of data, and the classification is performed based on Gaussian distribution parameters estimated by the fitting function [116]. Support vector machine (SVM) is based on Vapnik-Chervonenkis theory, where a hyperplane separating the classes is determined. SVMs are efficient algorithms suitable for compact datasets [117]. The nearest neighbor algorithm is based on the assumption that similar things exist nearby. It is a simple yet versatile model with high computational cost [118]. Ensemble methods such as bagged trees (or random forest) combine the predictions of several learning algorithms with improving generalization. Although these methods are also computationally expensive, they are unlikely to over-fit [119]. Regression analysis based on the above techniques was also performed alongside classification.

2.2.9 Performance Evaluation

Various performance evaluation metrics were utilized to compare different machine learning algorithms. The metrics used in this study include accuracy, sensitivity, specificity,

precision, recall, f-score, root mean squared error, and their corresponding mathematical formulations are given below.

The abbreviations used in the following expressions include True Positive (TP) which are the cases the model correctly predicted the positive (glaucomatous) class. True Negative (TN) are the cases the model correctly predicted the negative (non-glaucomatous) class. False Positive (FP) are the cases the model incorrectly predicted the positive (glaucomatous) class. False Negative (FN) are the cases the model incorrectly predicted the negative (non-glaucomatous) class.

2.2.9.1 Accuracy

Accuracy is the percentage of correctly classified observations, as shown below.

$$\text{Accuracy}(\%) = \frac{\text{TP} + \text{FP}}{\text{TP} + \text{TN} + \text{FP} + \text{FN}} \tag{2.3}$$

2.2.9.2 Sensitivity

Sensitivity/Recall estimates the proportion of actual positives (e.g. actual glaucomatous) was identified correctly.

$$\text{Sensitivity/Recall(RE)} = \frac{\text{TP}}{\text{TP} + \text{FN}} \tag{2.4}$$

2.2.9.3 Specificity

Recall estimates the model's ability to correctly reject healthy patients without a Glaucoma.

2.2.9.4 Precision

Precision estimates the proportion of positive predictions (e.g., glaucomatous predictions) that was actually correct.

$$\text{Precision(PR)} = \frac{\text{TP}}{\text{TP} + \text{FP}} \tag{2.5}$$

2.2.9.5 F-Score

The F-Score estimates the harmonic mean of the precision (PR) and recall RE.

$$\text{F} - \text{Score} = \frac{\text{PR} \times \text{RE}}{\text{PR} + \text{RE}} \tag{2.6}$$

where $(\text{PR}) = \frac{\text{TP}}{\text{TP+FP}}$ and $(\text{RE}) = \frac{\text{TP}}{\text{TP+FN}}$.

2.2.9.6 Root Mean Square Error (RMSE)

The Root Mean Square Error (RMSE) was used as the performance evaluation metric for regression analysis. RSME is the standard deviation of the prediction errors (residuals).

$$\text{RMSE} = \sqrt{\frac{\sum_{i=1}^{N} \left(\text{Actual}x_i - \text{Predicted}\hat{x}_i\right)^2}{N}} \tag{2.7}$$

Where N is the number of observations.

2.3 Results

A machine learning-based approach was developed and trained using the balanced ERG data previously published by Grillo et al. [81]. Although a compact dataset of 60

observations and 540 signals was used in this study, the current framework was able to consistently detect features (Figure 6 and Figure 9) that are known to be medically relevant such as OP, STR, Flicker reported in various studies [79, 81, 92, 120–122]. In particular, studies conducted by [123–125] investigating the variability of PhNR in glaucomatous and healthy subjects in PERG and fERG have found that PhNR to be an important biomarkers for detection of glaucoma. It is worth noting that in fERG analysis (ERG protocol for this study), pSTR, nSTR, PhNR are extracted from STR.

Therefore, we were able to demonstrate that the proposed framework for early-stage glaucoma diagnosis can be reproducibly evaluated and validated even on such a compact database. Furthermore, we would like to note that there are other investigations that successfully applied ML-based method in different fields, including biomedical [126] and material science [127] using compact datasets. The procedure employed for the development of the predictive modeling framework is summarized below.

- **Data Split:** Hold out (80% training, k-fold cross-validation, 20% testing).
- **Dimensionality reduction:** Feature Extraction.
- **Feature selection:** MRMR.
- **Hyper-parameter tuning:** k-fold cross-validation (k=10).
- **Model Evaluation:** Performance metrics evaluated on the unseen testing set.

The dataset was divided into two parts; 80% of the data was used for training and validation, and the remaining 20% was set aside for testing. The hold-out testing strategy

ensured that the test data was never a part of the training process [128]. Dimensionality reduction was performed using feature extraction and feature selection. MRMR feature selection algorithm was used to identify the important predictors. K-fold (K=10) cross-validation was used for training and hyper-parameter tuning [129]. The cross-validation technique significantly reduces bias when working with small datasets [130]. The loss function was the objective minimization function for both classification regressions during hyper-parameter optimization. The hyper-parameters associated with corresponding ML algorithms [131], as shown in Table 1, were optimized through nested cross-validation. Next, the trained model with optimized hyper-parameters was evaluated using test data that was not a part of training. To further ensure that the machine learning models compared in this investigation were not over-fitted, given the compact dataset used in the present study, the behavior of training and testing error vs. training cycles was monitored. Different techniques, including Tree, Discriminant, SVM, Naive Bayes, Tree Ensemble, and KNN, were applied, and their performances were assessed. The performance of each technique was assessed based on the accuracy (discussed in section Performance Evaluation) is tabulated in Table 2. Considering binary and multiclass classifications, it can be seen that the Ensemble-based technique (bagged tree) was consistently outperforming other techniques. Additionally, other performance metrics for ensemble bagged trees (discussed in section Performance Evaluation) are summarized in Table 3.

2.3.1 Binary Classification

For binary classification (classifying animals with/without glaucoma) based on statistical features, the correlation of cones, mean of flicker, median, and skewness of Hi

Rods and cones, and standard deviation of cones were identified as important among the statistical features as shown in Figure 4. Moreover, the box plot demonstrates variations of each feature for each class (with/without glaucoma), respectively. Several models, including SVM and ensemble-based classifiers were used for training, and their performances were assessed. It turned out that the SVM and ensemble bagged tree provide the best performance with a testing accuracy of 83.33%, as shown in Table 2.

Next, the binary classification was performed using wavelet-based features. Among the extracted wavelet features, Shannon Entropy Values for Maximal Overlap Discrete Wavelet Packet Transform (MOD-PWT) were identified as important features from Rods and cones, Rods, STR, and OP, as shown in Figure 5. The utilization of the selected advanced features improved the accuracy to 91.70% by the ensemble bagged tree algorithm.

It should be noted that the MRMR method selects features based on statistical relevance while dropping redundant features and thus, is computationally efficient [111, 112]. Figure 6. demonstrates this for binary classification. It can be observed that correlation feature from cones, Moment of order three and trimmed mean feature from Oscillatory Potentials (OP) and Range and aspect ratio from Scotopic Threshold Response (STR) are highly correlated; Therefore, only the feature cones correlation was picked by the MRMR algorithm as inclusion of the other three did not increase/decrease the models predictability.

Figure 7. compares the predictive importance scores obtained based on the statistical and wavelet-based features. Predictive importance scores describe the predictive capability of selected features [132]. It can be observed that wavelet-based features can

distinguish healthy and glaucomatous animals suggesting that they are more sensitive to subtle changes in ERG signals due to glaucoma. It should be noted that the feature selection algorithm MRMR (Maximum Relevance and Minimum Redundancy) ignores highly correlated features for model simplicity. Therefore, only uncorrelated sets of features that improved predictability across the animals were chosen, i.e., for a set of correlated features, one representing the correlated set gets picked by the algorithm. Figure 6. demonstrates the list of important but highly correlated features that were dropped. The scatter plot inside the Figure 6 shows the correlation coefficients confirming the high degree of the correlation between them.

2.3.2 Multiclass Classification

For multiclass classification (classifying animals to different stages, normal, high, and glaucomatous as mentioned in Dataset section) based on statistical features, the correlation of cones, number of troughs in Hi cones, kurtosis of STR and mean of flicker were identified as important among the statistical features as shown in Figure 8. Several models, including SVM and ensemble-based classifiers, were used for training, and their performances were assessed. It turned out that the ensemble-based classifiers, specifically the bagged trees model, provided the best performance with a testing accuracy of 53.33%, as shown in Table 2.

Next, the multiclass classification was performed using wavelet-based features. Among the extracted wavelet features, Wavelet variance of rods and Shannon Entropy Values and AR coefficients for Maximal Overlap Discrete Wavelet Packet Transform (MOD-PWT) were identified as important features from Hi-Flicker, Flicker, Hi-cones, and

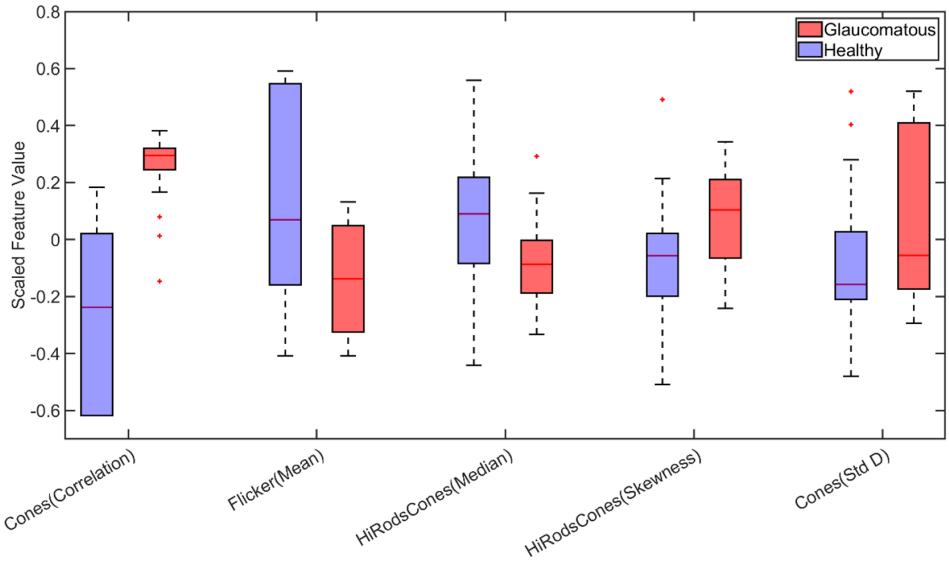

Figure 4: Boxplot of statistical features selected by Minimum Redundancy and Maximum Relevance (MRMR) feature selection algorithm for binary classification. (Abbreviations: Std D: Standard Deviation), On each box, the central mark indicates the median, and the bottom and top edges of the box indicate the 25th and 75th percentiles, respectively. The whiskers extend to the most extreme data points not considered outliers, and the outliers are plotted individually using the '+' marker symbol.

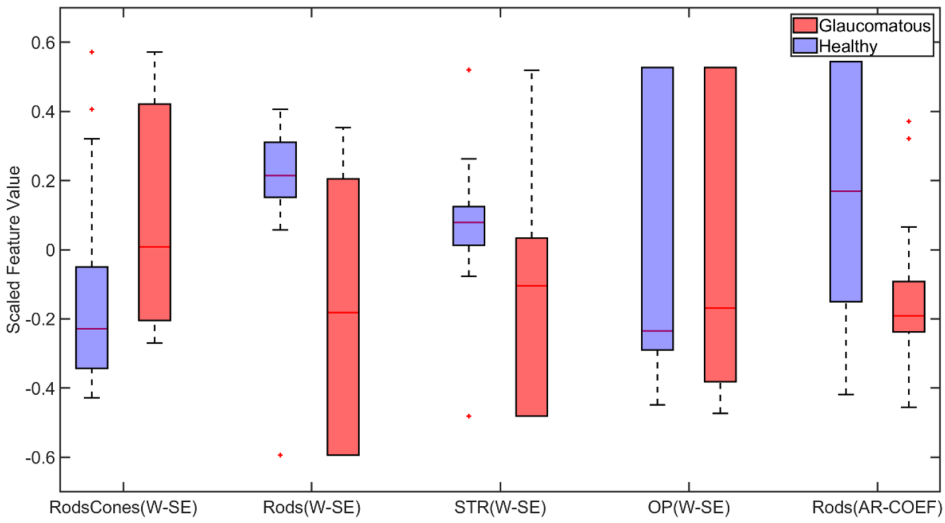

Figure 5: Box plot of wavelet-based features selected by Minimum Redundancy and Maximum Relevance (MRMR) feature selection algorithm for binary classification. (Abbreviations: W-SE: Wavelet based Shannon Entropy, AR-COEF: Autoregressive Coefficient), On each box, the central mark indicates the median, and the bottom and top edges of the box indicate the 25th and 75th percentiles, respectively. The whiskers extend to the most extreme data points not considered outliers, and the outliers are plotted individually using the '+' marker symbol.

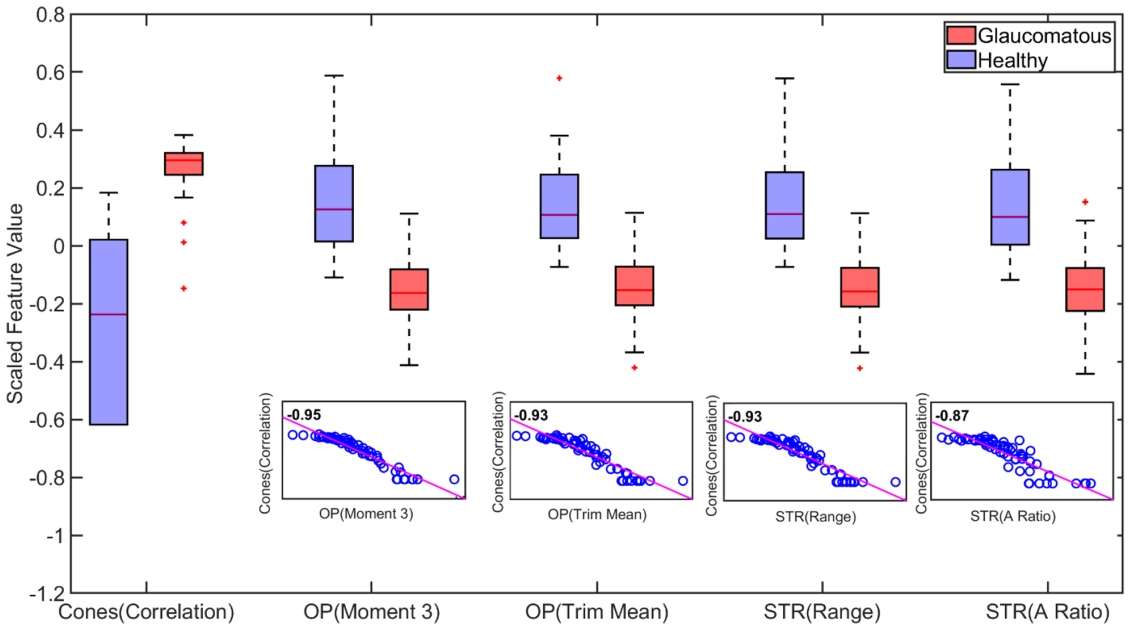

Figure 6: Boxplot of statistically important features for binary classification. The important features capable of distinguishing healthy and glaucomatous are correlated feature from Cones, third order Moment and trimmed mean feature from Oscillatory Potentials (OP) and Range and aspect ratio from Scotopic Threshold Response (STR). However, the high similarity between these features quantified by the correlation scores in the scatter plot create redundancy (inclusion cones(correlation) feature alone vs inclusion all five features does not improve accuracy). Therefore, utilizing the cones correlation feature alone captures the behavior of the other four features. This dropping of redundant features and choosing Cones(correlation) feature alone is achieved by using Minimum Redundancy and Maximum Relevance (MRMR) algorithm. (On each box, the central mark indicates the median, and the bottom and top edges of the box indicate the 25th and 75th percentiles, respectively. The whiskers extend to the most extreme data points not considered outliers, and the outliers are plotted individually using the '+' marker symbol.)

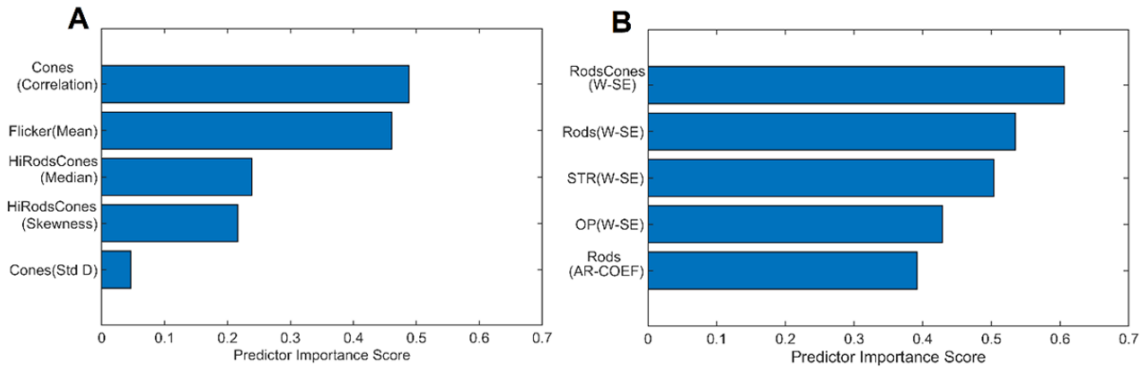

Figure 7: Comparison of predictive importance scores for binary classification using (A) Statistical features and (B) wavelet-based features. This bar chart illustrates the superior predictive capability of wavelet-based features. (Abbreviations: Std D: Standard Deviation, W-SE: Wavelet based Shannon entropy, AR-COEF: Autoregressive coefficient)

STR as shown in Figure 9. The identification of flicker as an important distinguishing feature in diagnosing early-stage glaucoma was consistent with previous studies [122, 133–135]. In fact, flicker measurements in eyes with early-stage glaucoma exhibited a loss in sensitivity around 30 Hz to 40Hz [122]. It is worth noting that the flicker measurements used in this study were recorded using flashes at 30 Hz. The identification of the flicker ERG test and the corresponding features, among other tests, reconfirmed the capability of the current approach in identifying the relevant features. Training the ensemble bagged trees model, utilizing the selected advanced features, improved the multiclass classification accuracy to 80%, as shown in Table 2. This improvement in accuracy indicated that wavelet-based features can distinguish healthy and glaucomatous animals suggesting that they are more sensitive to subtle changes in ERG signals due to glaucoma. The multiclass classification ability of this framework reaffirmed the rich and complex nature of ERG signals in assessing the disease progression.

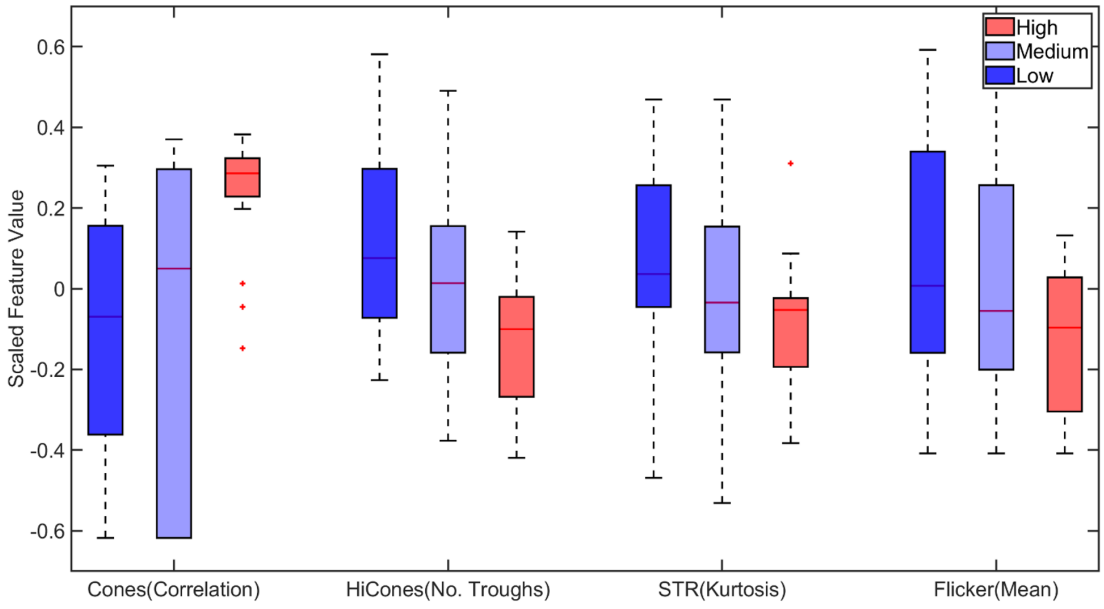

Figure 8: Boxplot of statistical features selected by Minimum Redundancy and Maximum Relevance (MRMR) feature selection algorithm for multiclass classification. (Abbreviations: STR: Scotopic Threshold Response). On each box, the central mark corresponds to the median, and the bottom and top edges of the box correspond to the 25th and 75th percentiles, respectively. The dashed lines (whiskers) extend to the most extreme data points not considered outliers, and the outliers are plotted individually using the '+' marker symbol.

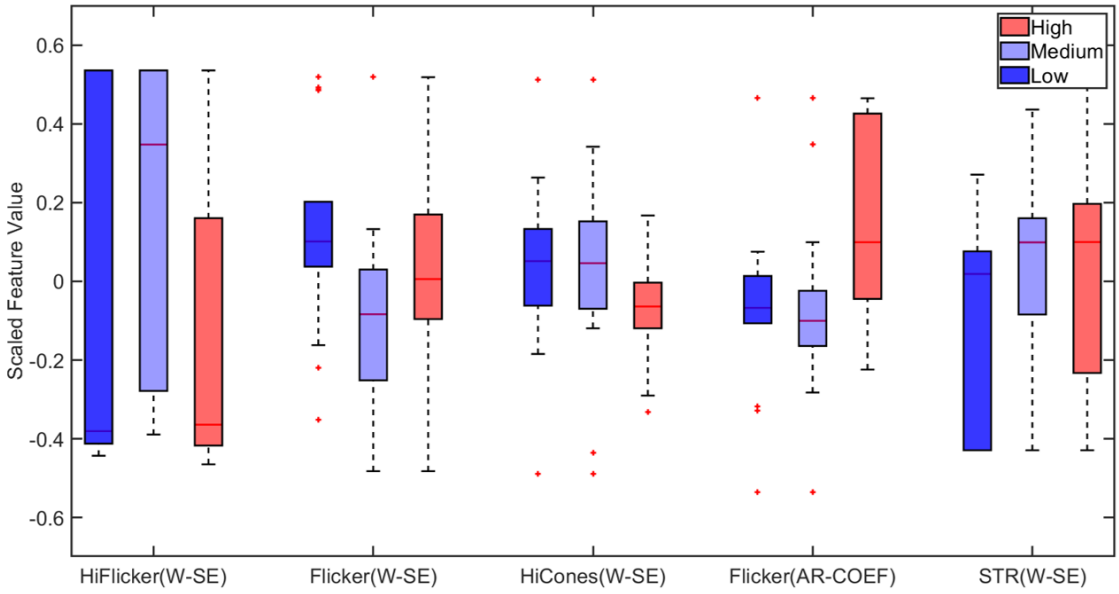

Figure 9: Boxplot of wavelet-based features selected by Minimum Redundancy and Maximum Relevance (MRMR) feature selection algorithm for multiclass classification. (Abbreviations: STR: Scotopic Threshold Response, W-SE: Wavelet based Shannon Entropy, AR-COEF: Autoregressive Coefficient). On each box, the central mark indicates the median, and the bottom and top edges of the box indicate the 25th and 75th percentiles, respectively. The whiskers extend to the most extreme data points not considered outliers, and the outliers are plotted individually using the '+' marker symbol.

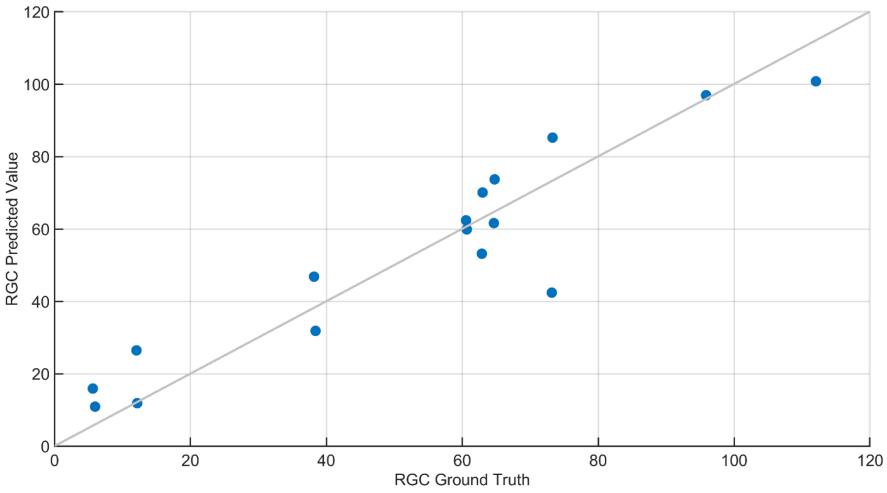

Figure 10: RGC count regression plot. This plot contains the ground truth and predicted response of RGC count predicted using Gaussian Process Regression (GPR). The squared exponential GPR model was trained using both standard and advanced features. The RGC count of the animals ranged between 8 and 120, and the root mean squared error in the prediction of RGC was 11.2. The line in this plot denotes when the predicted values are equal to ground truth values.

2.3.3 RGC Regression

Regression analysis was performed to predict retinal ganglion cell count from ERG signals. Feature selection for regression was performed using MRMR sequential feature selection. RGC values of the animals ranged between 8-120. RSME for RGC regression was 15.64 and 11.20 for models trained with statistical features and wavelet-based features, respectively. Regression results using wavelet-based features are shown in Figure 10. The results in [81] indicate that RGC counts had a strong correlation with STR and OPs. The dominant features selected for RGC regression (from STR and OP) were in agreement with the findings in [81]. Table 4. compares performance of various ML based regression models in predicting retinal ganglion cells (RGCs) counts: The higher error (RSME) with statistical features compared with the wavelet-based advanced features emphasized the need for sophisticated features to predict RGC count accurately. SVM- and GPR-based models provided the most accurate prediction of RGC numbers from ERG signals. Specifically, squared exponential and rational quadratic models of GPR provided the least error.

2.4 Discussion

Our goal was to determine the feasibility of applying ML-based methods to the analysis of ERG signals for glaucoma detection at different stages of the disease. In the present study, we systematically applied machine-learning-based methods for the first time to detect glaucoma and predict RGC loss based on ERG signals. The present study utilized ERGs measured in mice rather than from human patients, because the use of data

from a preclinical model allowed us to validate 'ground truth' data sets with a range of complimentary and alternative experimental strategies, which is not possible in human clinical studies. These include histology, biochemical and immunochemical assays, as well as optomotor reflex measurements. We were able to determine for the first time that advanced features (wavelet-based features) are capable of detecting subtle changes in the ERG signal and perform multiclass classification based on the progression level of the disease with 80% accuracy. In particular, we found that Shannon Entropy Values for Maximal Overlap Discrete Wavelet Packet Transform (MOD-PWT) and AR coefficients represent important features capable of detecting early-stage glaucoma. Among the nine available ERG signals, Flicker, STR, OP, and Rod-Cone appear integral for such successful detection. This is in agreement with the results published in [76]. However, given that these features are highly correlated, the ML-based algorithm picks only one for each set of highly correlated features to reduce the model complexity as shown in Figure 6.

In addition, the method proposed here performs ERG analysis in a wavelet domain instead of a frequency domain, which allows to capture subtle changes in the signals. In addition, various intricate features such as multiscale wavelet variance estimates, Shannon entropy, and autoregressive coefficients are incorporated in the method, compared to basic features such as differences in amplitude and latency in previous studies [20,48–59,65]. The results strongly suggest that such advanced features in the wavelet domain are necessary for detection of early-stage glaucoma. Moreover, in contrast to the recent study that leverages ML-based technique to analyze ERG using solely the photopic negative response (PhNR) component [66], the current method uses all ERG components in the analysis to

fully utilize the capability of the ML-based technique to crunch large data sets and draw complicated relationships. Therefore, the proposed framework is not limited to a small subset of genetic eye diseases like previous studies [49–59, 65]; instead, it is capable of mapping ERG signals to various eye diseases.

2.4.1 Conclusion

Results obtained in the present study strongly suggest that the methods employed can reproducibly identify dominant features for classification and regression from STR, Oscillatory potentials (OPs), and other ERG tests consistent with the results reported in previously published work on the sensitivity of and OPs and flicker to subtle changes in RGC function and viability [14, 122]. Further, our approach identified additional dominant distinguishing features such as Shannon Entropy Values for Maximal Overlap Discrete Wavelet Packet Transform (MOD-PWT) and AR coefficients, which are not distinguishable by traditional methods used in [81]. This strongly suggests that the current machine-learning-based algorithm has significant potential in distinguishing subtle changes in ERG signals corresponding to different stages of glaucoma disease development. This capability of the technique could be used as a foundational step to create a reliable framework for the early detection of glaucoma and to monitor efficacy of therapeutic intervention in both clinical practice and novel drug development for glaucoma. In addition, the inclusion of various ERG protocols in this framework, such as cones, rods and cones, STR, and oscillatory potentials, represent responses from different cell types in the eye. Therefore, ERG response can be mapped to diseases specific to those cell types. It should be noted that this study was based on mice and with 12 hours of dark adaptation. The promising results obtained here suggest the great potential for this method to help detect early stage, pre-symptomatic glaucoma. However, an additional study on adaptation requirements would be required before extending this framework to humans.

Table 1: Hyperparameters Tested/Optimized

Method	Hyperparameter Search Range	Optimized Hyperparameters
Ensemble	**Ensemble method:** Bag, GentleBoost, LogitBoost, AdaBoost, RUSBoost **Number of learners:** 10-500 **Learning rate:** 0.001-1 **Maximum number of splits:** 1-47 **Number of predictors to sample:** 1-5	**Ensemble method:** Bag **Maximum number of splits:** 1 **Number of learners:** 52 **Number of predictors-to sample:** 1
Knn	**Number of neighbors:** 1-24 **Distance metric:** City block, Chebyshev, Correlation, Cosine, Euclidean, Hamming, Jaccard, Mahalanobis, Minkowski (cubic), Spearman **Distance weight:** Equal, Inverse, Squared inverse **Standardize data:** true, false	**Number of neighbors:** 24 **Distance metric:** Correlation **Distance weight:** Inverse **Standardize data:** true
NaiveBayes	**Distribution names:** Gaussian, Kernel **Kernel type:** Gaussian, Box, Epanechnikov, Triangle	**Distribution names:** Gaussian **Kernel type:** Epanechnikov
Discriminant	**Discriminant type:** Linear, Quadratic, Diagonal Linear, Diagonal Quadratic	**Discriminant type:** Diagonal Linear
SVM	**Multiclass method:** One-vs-All, One-vs-One **Box constraint level:** 0.001-1000 **Kernel scale:** 0.001-1000 **Kernel function:** Gaussian, Linear, Quadratic, **Cubic Standardize data:** true, false	**Kernel function:** Linear **Box constraint level:** 2.4185 **Multiclass method:** One-vs-All **Standardize data:** false
Tree	**Maximum number of splits:** 1-47 **Split criterion:** Gini's diversity index, Maximum deviance reduction	**Maximum number of splits:** 5 **Split criterion:** Maximum deviance reduction

Table 2: Testing accuracy obtained using various machine learning techniques. (Bold font indicate the accuracies of best performing classifier.)

		Tree	**Discriminant**	**SVM**	**Naive Bayes**	**Ensemble (Bagged)**	**KNN**
Binary	**Statistical**	75	80	**83.33**	80	**83.33**	66.70
	Wavelet	83.33	83.33	**91.70**	83.33	**91.70**	75
Multiclass	**Statistical**	33.33	41.70	50	16.70	**53.33**	33.33
	Wavelet	41.70	50	64.66	33.33	**80**	50

Table 3: Performance Metrics for Ensemble Classifier.

		Accuracy	**F-Measure**	**Precision**	**Sensitivity**	**Specificity**
Binary	**Statistical**	80	80	80.36	80.36	80.36
	Wavelet	91.67	91.61	92.86	91.67	91.67
Multi-Class	**Statistical**	53.33	50.74	53.18	51.67	75.48
	Wavelet	80	79.63	83.81	83.333	90.30

Table 4: Performance Metrics for retinal ganglion cells (RGCs) Regression. (Bold font indicate the best performing regression model and its corresponding RSME.)

Machine Learning Algorithm	**RSME**	
	Statistical	**Wavelet**
Tree	31.716	17.852
SVM	17.177	13.82
Ensemble (Bagged)	29.129	24.387
Logistic Regression	44.622	24.873
Gaussian Process Regression	**15.644**	**11.201**

CHAPTER 3

CASE STUDY 2: NOVEL MACHINE-LEARNING-BASED STALL DELAY CORRECTION MODEL FOR IMPROVING BLADE ELEMENT MOMENTUM ANALYSIS IN WIND TURBINE PERFORMANCE PREDICTION

3.1 Introduction

The rapid depletion of fossil fuels in recent decades has resulted in a scarcity of power generation. This intensifies the demand for alternate energy sources to fossil fuels. Wind energy has been acknowledged as one of the most intriguing renewable energy resources [136]. Wind turbine design is demanding in terms of both expense and time. Based on this, the engineering approach known as blade element momentum (BEM) was extensively employed in wind turbine blade design [137–139]. With the increasing dimensions of wind turbine blades, precise and efficient techniques for predicting aerodynamic loads and performance are anticipated [140]. The BEM method evaluates forces throughout the blade length and ultimately the torque and the engendered power by the rotor depending on wind speed, rotor design, and aerofoil characteristics (C_L and C_D). Since wind turbine cross-sections are aerofoil-shaped, the BEM method requires aerofoil characteristics in order to evaluate sectional aerodynamic forces [139]. At low wind speeds, BEM predictions exhibit good accuracy, but at higher wind speeds, BEM fails due to massively separated flow conditions [139, 141]. The characteristics of the aerofoil used in BEM are predicted from a 2D wind tunnel or CFD measurements [139, 142]. Owing to the spanwise separated flow, there is an enhancement in the lift coefficient of the aerofoils of the rotating blade at

the identical angle of attack compared to the 2D analysis of the aerofoil or 3D analysis of the aerofoil of a non-rotating blade, which delays stall. This phenomenon is called "stall delay". [138, 139]. There is no conclusive knowledge regarding the causes of stall delay, however it is thought that when flow separation begins, a separated air mass on the suction face rotates with the blade due to centrifugal force. The separated air mass tends to approach the tip radially due to centrifugal force. This spanwise flow therefore enables Coriolis force to impact toward the trailing edge, resulting in a delay in stall initiation [139–141, 143–148]. The second explanation in the literature [140, 147, 149] that contributes for the radial flow of the separated air mass is the dynamic pressure gradient along the length of the blade. Eventually, stall delay is a boundary layer impact that is speculated to be induced by centrifugal force, dynamic pressure gradient, or a blend of the two. Although technologically advanced wind turbines are pitch-controlled and therefore do not normally function in stall, stall in the inner section of the blade is inevitable once rated power is reached [150]. Failure to comprehend the effect of stall delay may lead to under-prediction of aerodynamic values and design failure. It is more effective at inboard portions and progressively drops towards the tip [139]. As a corollary, before utilising them in design, 2D aerofoil characteristics must be compensated for rotational impacts [139, 140].

Himmelskamp [151] in the 1940s was the first to recognize the difference between lift coefficients for rotating and non-rotating aircraft propellers. Banks and Gadd [152] conducted a theoretical study and clarified how rotation delays separation and inferred that rotation induces the boundary layer to stabilize and resist separation. Stall delay

was analysed and examined by Dwyer and McCroskey [153] on helicopter rotors. Later, in wind turbines, Milborrow [154] and Madsen and Christensen [155] noticed the stall delay effect. Variation in the predicted lift coefficient comparing rotating and non-rotating blades was shown by Ronsten [1] in his observational investigation. Figure 11 presents the estimated lift coefficient at 30 percent of the blade length from the work of Ronsten [1].

Wood [156], Narramore and Vermeland [157], and Snel et al. [158] conducted CFD evaluation in the early 1990s, with development of computers, to examine the consequences of stall delay. Numerous empirical correction models for wind turbine rotor design have been generated over the last few decades [139, 146, 150]. These were all three-dimensional correction models considering the impact of stall delay to correct 2D aerofoil characteristics. In 2001, NREL performed a blind test comparison relying on an interpretation of the experimental results from an NREL Phase VI turbine. Experts were urged to estimate the load values for the NREL Phase VI turbine without the actual experimental results being given to them [159]. Significant uncertainties were reported as compared with experimental results and estimated values.

Consequently, existing models to modify 2D aerofoil characteristics to depict stall delay effects were found to be incorrect. In 2002, Schreck and Robinson [149], using the results of the NREL Phase VI turbine experiment, utilised CFD to examine the influence of the radial pressure gradient on the stall delay mechanism. In 2008, in simulating the NREL Phase VI turbine, Breton et al. [146] utilised the lifting line-prescribed wake vortex theory to explore the performance of six correction models for stall delay (Snel, Chaviaropoulos and Hansen, Raj, Corrigan and Schilling, Bak, and Lindenburg models) and hypothesized

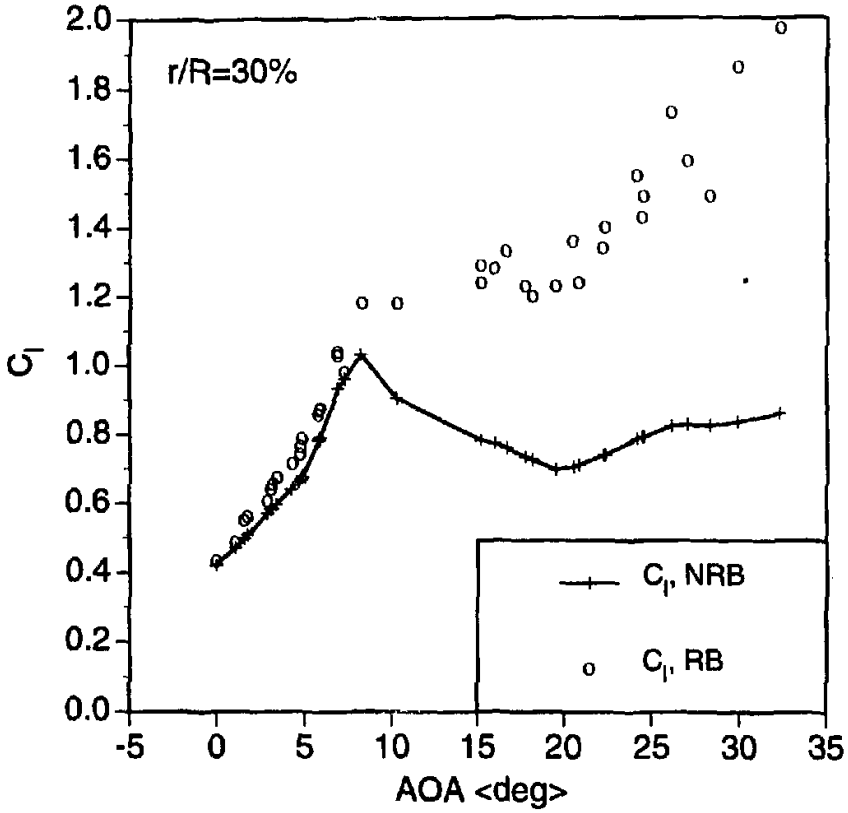

Figure 11: C_L vs. AoA for rotating blade (RB) and non−rotating blade (NRB) at 30 percent blade length [1].

that all these models end in over-prediction. Guntur et al. [150] conducted an equivalent test for the MEXICO rotor, and the selected correction models (Snel, Du and Selig, Chaviarpoulus and Hansen, Lindenburg, and Bak) failed to predict the 3D aerodynamic characteristics accurately. In prior work, the authors Kabir and Ng [139] compared 3D aerofoil coefficients computed throughout the blade length from NREL Phase VI turbine CFD simulation with values computed utilising BEM analysis employing four correction models (Snel, Lindenburg, Du and Selig, and Chaviarpoulus and Hansen models). It was found that these models over-predicted the lift coefficients and power computed, especially at high wind speeds. This was predominantly owing to the complexity of foreseeing the rotation effect on wind turbines, stressing the importance of developing an accurate numerical model. Guntur and SÃ¸rensen [150, 160] used the Inverse BEM method to compute the angles of attack and the 3D aerofoil characteristics of the specific segments of turbine blades. Lately, Kabir and Ng [139] enhanced the Inverse BEM strategy as well as the computed angle of attack and 3D aerofoil characteristics of 18 Sections (5 sections regarded for experimental measurements and 13 additional sections as outlined in blade design) from full rotor CFD simulations of the NREL Phase VI turbine. Kabir and Ng [139] also proposed amendments to BEM analysis to account for the impact of local blade length using the angle of attack and aerofoil characteristics computed from Inverse BEM evaluation. Regrettably, the main purpose of using BEM analysis is pace and ease. Although the method of computing 3D aerofoil characteristics is precise, it is complex and requires substantial computational power to model CFD and perform Inverse BEM. Therefore, an optimal method must be established to reconcile precision and pace.

In this paper, a new empirical model derived from the soft computing technique called 'Symbolic Regression' is formulated for the correction of 2D aerofoil characteristics data to compensate for the stall delay in wind turbine blade design and performance analysis via BEM. This paper is structured as follows:

1. A synopsis of the stall delay mechanism;
2. A synopsis of the Blade Element Momentum theory and Inverse BEM theory;
3. A brief description of existing correction models for stall delay used in BEM;
4. Description of the NREL Phase VI turbine and MEXICO rotor experiments;
5. Proposed new models;
6. Results comparison to NREL Phase VI turbine and MEXICO rotor data, followed by discussion.

3.2 Stall Delay Mechanism

Stall delay is a boundary layer phenomenon that is primarily assumed to be attributable to centrifugal force, a dynamic pressure gradient, or a blend of both. Either or both of these responses stimulate spanwise flow, leading to formation of the Coriolis force [2,3,139–141,143–149,161], as shown in Figure 12. The Coriolis force acts from the leading edge to the trailing edge as a positive chord-wise pressure gradient, ensuing in stall delay, as shown in Figure 13. Figure 13 illustrates this phenomenon, where the pressure difference between the aerofoil's suction side and pressure side is higher for a rotating flow

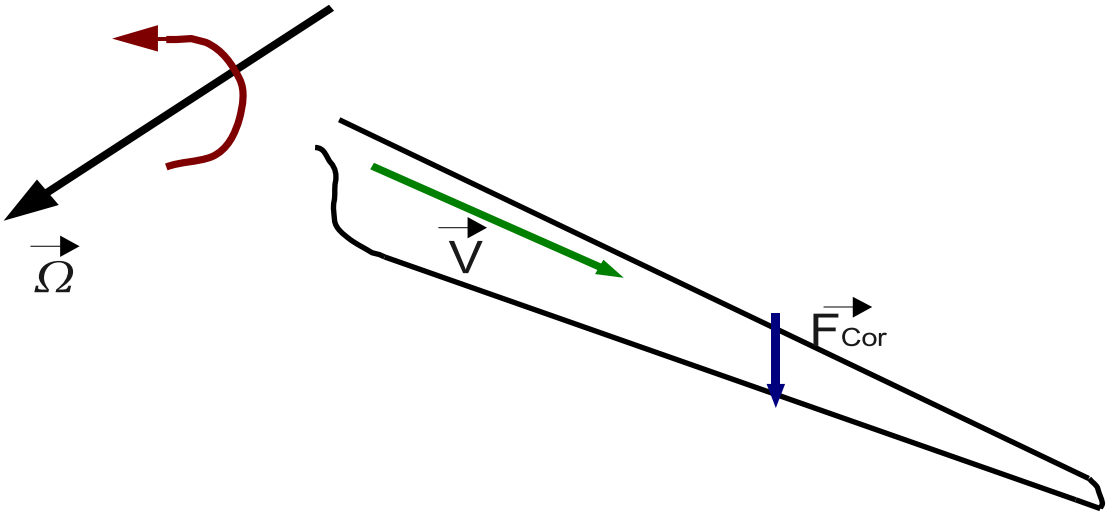

Figure 12: Stall delay phenomenon [2].

than for a non-rotating flow due to the presence of Coriolis force, which increases the lift coefficient. At low wind speeds, which implies low angles of attack, the flow stays attached on the rotor's suction side, and no stall emerges. Even though centrifugal force and the dynamic pressure gradient are present, their effects are modest since the flow passes over the blade in a brief period of time. When flow separation occurs at higher wind speeds (i.e., at higher angles of attack), a separated air mass persists along the suction surface and is subjected to centrifugal pumping and/or a dynamic pressure gradient. When spanwise flow occurs in a rotating reference frame, the Coriolis effect occurs, resulting in stall delay.

3.3 Blade Element Momentum Theory and Inverse BEM Theory

3.3.1 Blade Element Momentum Theory

Due to its simplicity and speed, the Blade Element Momentum (BEM) method is often utilised for wind turbine blade design and wind turbine performance analysis. The

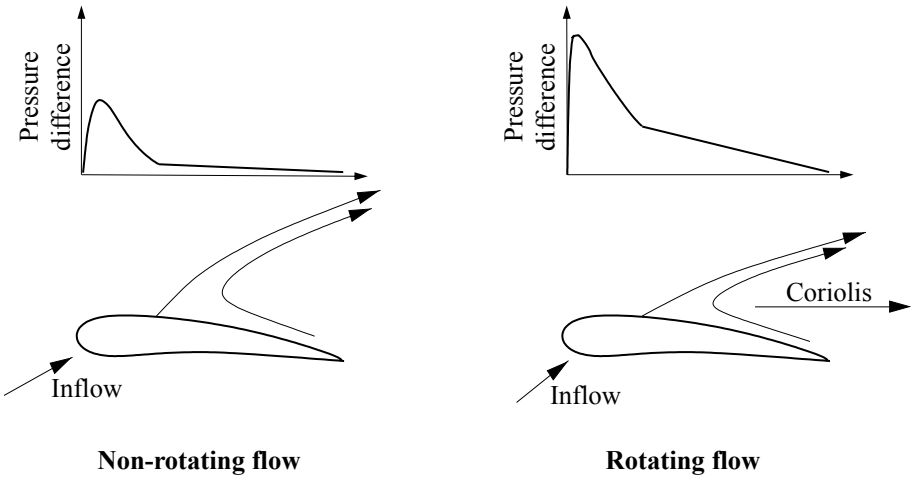

Figure 13: Favourable pressure gradient due to the Coriolis force in rotating flow (inspired from [3]).

BEM methodology estimates forces throughout the blade length and ultimately the torque and the turbine power. Betz's [162] and Glauert's [163] research serve as the foundation for this concept. The BEM theory blends the concepts of momentum and blade element theories into one cohesive framework. The momentum balance on a rotating annular stream tube is described using the momentum theory, while the forces created by the aerofoil cross-section of the blade section are computed using the blade element theory. In BEM theory, a wind turbine blade is segmented into (N) elements. The intent is to establish a balance between the force imposed on the blade elements and the change of the momentum magnitude of the air between the upstream and downstream regions of the rotor based on these two theories in each element independently. In Burton et al. [143] and Hansen [164], the BEM method is properly delineated. The fundamental premise of BEM theory is that forces and velocities computed in each element are calculated independently and are unaffected by the adjacent elements. The aerofoil characteristics (C_L and C_D)

required by the blade element theory to calculate forces at each sectional element are generally obtained via wind tunnel or 2D CFD simulations. The three-dimensional (3D) and unsteady effects happening on the blade, such as yaw misalignment, wind shear, tower shadow, dynamic stall, dynamic inflow, and stall delay, cannot be captured directly by the BEM method [161, 164–166]. The other effects are real-time, while the stall delay explained earlier raises the lift coefficient even under ideal conditions owing to blade rotation. Thus, it is necessary to first enhance BEM to take into account stall delay, followed by the inclusion of corrective models for additional real-time unsteady effects. In synopsis, traditional BEM theory is based on two-dimensional aerofoil characteristics that must be rectified for the rise in value caused by stall delay.

3.3.2 Inverse Blade Element Momentum Theory

The authors earlier [139] provided a comprehensive description of BEM analysis of the NREL Phase VI turbine using several aerofoil characteristic extrapolation techniques and different existing correction models for stall delay. The authors demonstrated that it is crucial to determine the optimal aerofoil characteristics ($C_{L,3D}$ and $C_{D,3D}$) throughout the blade length in order to improve the BEM model and narrow the disparity among 2D and 3D aerofoil characteristics. The computation of sectional AoA, $C_{L,3D}$, and $C_{D,3D}$ throughout the blade length has been accomplished using a variety of methodologies [160, 167]. One of the strategies is the Inverse BEM method. This was a strategy utilised by the authors. In previous work [139], the authors validated their computation using other approaches used by other researchers to estimate the sectional $C_{L,3D}$ and $C_{D,3D}$ for the NREL Phase VI turbine. Inverse BEM analysis is carried out in the opposite way from BEM analysis,

as the name indicates. In the conventional BEM analysis outlined above, at each element, based on the calculated AoA, $C_{L,2D}$, and $C_{D,2D}$, is supplied as key to determine the forces impacting that element. While in Inverse BEM analysis, the forces calculated from 3D CFD or experimental analysis were used to predict the aerofoil characteristics ($C_{L,3D}$ and $C_{D,3D}$) using the reverse approach to BEM [139].

3.4 Models for Stall Delay Correction in BEM Technique

The BEM process utilises the aerofoil sections' C_L and C_D values throughout the blade length. Aerofoil characteristics are typically inferred from wind tunnels or 2D CFD tests. As stated in the preceding section, stall delay enhances C_L, notably on the inboard portions of the blade. There are numerous correction models to integrate BEM analyses to account for the impact of stall delay. The inaccuracies of various correction models for stall delay were outlined in Section 3.1. Breton et al. [146] compared the results of the NREL Phase VI turbine to six correction models for stall delay: Snel [168], Chaviaropoulos and Hansen [169], Raj [170], Corrigan and Schilling [171], Bak [172], and Lindenburg [144]. The models over-predicted the forces observed on a wind turbine blade throughout a variety of operating cases, while the model built by Lindenburg [144] was shown to perform the best across the set of scenarios investigated but still had substantial inadequacies. Guntur et al. [150] did an analogous test for the MEXICO rotor and compared it to five correction models: Snel [168], Du and Selig [173], Chaviarpoulus and Hansen [169], Lindenburg [144], and Bak [172]. None of the five correction models could accurately predict the 3D aerofoil characteristics [140, 150]. Detailed assessments of the

BEM analysis for the evaluation of the NREL Phase VI turbine were carried out in 2017 by Kabir and Ng [139]. They focused on the various extrapolation methods for the S809 aerofoil polar characteristics. They used an enhanced Inverse BEM strategy to predict $C_{L,3D}$ and $C_{D,3D}$ values from the full CFD rotor analysis throughout the blade length and compared their measured values with the corresponding BEM values, leveraging four different correction models for stall delay [139]: Snel [168], Du and Selig model [173], Chaviaropolous and Hansen [169], and Lindenburg [144]. It was observed that among the four models, the Lindenburg model was closest to the lift coefficients predicted by the Inverse BEM analysis of the 3D CFD simulation of the NREL Phase VI turbine.

Based on the disparity between 3D and 2D values and the use of symbolic regression as a soft computation methodology, a new correction model for stall delay is established in this work. Section 3.6 gives a brief synopsis of symbolic regression and the new model. It has previously been determined from three prior reports [139, 146, 150] that existing correction models for stall delay—Snel [168], Du and Selig [173], Chaviaropolous and Hansen [169], Raj [170], Corrigan and Schilling [171], and Bak [172]—are inaccurate; thus, these models are discarded for comparison in this study. Since the Lindenburg [144] model was determined to be the closest to the 3D lift coefficient among all models [139, 146], it is used for comparison with our novel model. The general formulation for the correction models are given below:

$$C_{L,3D} = C_{L,2D} + f_L \left(2\pi \left(\alpha - \alpha_0\right) - C_{L,2D}\right) \tag{3.1}$$

$$C_{D,3D} = C_{D,2D} + f_D \left(C_{D,2D} - C_D(\alpha = 0)\right) \tag{3.2}$$

where α_0 is the AoA when the lift is zero, and $C_D(\alpha = 0)$ is the drag coefficient when AoA is zero. In this article, we have also included two additional recent correction models for stall delay for comparison. The three models used for comparison in this present study are:

3.4.1 Lindenburg [144]

Lindenburg analysed the stall delay phenomenon thoroughly and inferred that centrifugal pumping was its primary cause. In addition, he developed a stall delay correction model based on centrifugal pumping. In his correction model, he extended the model developed by Snel et al. [158] by including the ratio of the rotational speed at the tip and the relative local velocity. However, he did not provide a correction model for drag.

$$f_L = 3.1 \left(\frac{\Omega r}{U_{rel}} \right)^2 \left(\frac{c}{r} \right)^2 \tag{3.3}$$

$$f_D = 0 \tag{3.4}$$

3.4.2 Dumitrescu and Cardos [174–176]

A semi-empirical model for rectifying the two-dimensional lift coefficient of aerofoils was built by Dumitrescu and Cardos. This model fails to rectify the drag coefficient correction.

$$f_L = \left[1 - \exp\left(-\frac{\gamma}{r/c - 1} \right) \right], \quad \gamma = 1.25 \tag{3.5}$$

$$f_D = 0 \tag{3.6}$$

3.4.3 Hamlaoui, Smaili and Fellouah Model [177]

This model was developed on the basis of an evaluation conducted between the two-dimensional lift coefficients and the NREL Phase VI turbine experimental results. This model also fails to rectify the drag coefficient correction.

$$f_L = ae^{-(\frac{\alpha-b}{c})^2} \tag{3.7}$$

$$C_{L,3D} = C_{L,2D} + f_L(C_{L,2D}) \tag{3.8}$$

where a, b, and c are constants, and α is the effective angle of attack (radian). For spanwise positions below 0.30R, a is 1.45, b is 0.7, and, c is 0.2832. Constant a is 0.55, b is 0.3826, and c is 0.1188 for spanwise positions higher than 0.30R.

3.5 Description of Experiments of NREL Phase VI Turbine and MEXICO Rotor

3.5.1 NREL Phase VI Turbine Experiment

The NREL Phase VI turbine (10.06 m in diameter) is a two-bladed HAWT that has been rigorously evaluated in the NASA Ames 24.4 m $\times$ 36.6 m wind tunnel in a series of operating scenarios [178]. Throughout the span of the blade, the blades are tapered and twisted and incorporate an S809 aerofoil. A consistent rotational speed of nearly 72 revolutions per minute (rpm) was maintained regardless of the wind speed. The sectional pressure distributions were monitored using 22 pressure taps interspersed at five radial positions: 30 percent, 47 percent, 63 percent, 80 percent, and 95 percent of the span. The sectional normal and tangential forces were evaluated by summing the surface pressures at all 22 of these points at each radial position. The technical report [178] has

more specific details of the experiment. The experimental data from Sequence S with an axial inflow condition was/is utilised in the authors' prior and current research. In a previous study [139], unsteady RANS (URANS) CFD simulations were conducted by the authors for inflow wind speeds of 7 m/s, 10 m/s, 15 m/s, 20 m/s, and 25 m/s employing the advanced sliding mesh method. $C_{L,3D}$ and $C_{D,3D}$ were calculated by employing Inverse BEM analysis at 18 radial positions (supplementary to the five radial positions used for experimental investigations, thirteen other positions were examined).

3.5.2 MEXICO Experiment

The Mexnext Phase III project was a global partnership led by the Netherlands' Energy Research Centre (ECN) [179]. In 2018, the findings of the NEW MEXICO experiment, which was conducted in the German–Dutch wind tunnel, DNW, with an open section measuring 9.5 m $\times$ 9.5 m, became accessible [179]. The MEXICO rotor blade is 4.5 m in diameter and is composed of three aerofoils: DU91-W2-250, RISØ-A2-21, and NACA 64-418, from 20 to 45.6 percent of blade length, 54.4 to 65.6 percent of blade length, and 74.4 to 100 percent of blade length, respectively. The entire blade is twisted and tapered, with a global pitch angle of -2.3°. Experiments were conducted in the wind tunnel at 10 m/s, 15 m/s, and 24 m/s with the blade rotating at 425.1 rpm. Axial inflow was taken into account in this analysis, and the influence of blade yaw was not considered. The pressure was measured using pressure sensors positioned at five distinct blade sections: 25 percent, 35 percent, 60 percent, 82 percent, and 92 percent of the blade length. The authors in their previous work [180] used the sliding mesh approach to perform both Unsteady RANS (URANS) and LES CFD analysis for inlet wind speeds of 10 m/s, 15 m/s, and 24

m/s.

3.6 Symbolic Regression

Artificial intelligence (AI) is gaining popularity in several fields, from basic domestic appliances such as washing machines to advanced automated medical diagnosis [46, 181–183]. The behaviour of AI is close to that of the human brain and can draw conclusions primarily based on constrained and particular facts from earlier studies [184]. Soft computing is a subset of artificial intelligence that deals with methods for conducting predicted qualitative and logical cognition [184, 185]. Zadeh [186] coined the word "soft computing" to describe an alternate to traditional (hard) computing. Hard computation is a traditional problem-solving strategy that involves specifically defined computational or mathematical models, which requires a long period of computing and is inefficient in many complex real-world scenarios [185, 187, 188]. Evolutionary computation, fuzzy logic, probabilistic reasoning, neural networks, expert systems, data mining, and machine learning are some of the most important soft computational methods or techniques [185, 188, 189]. In this research, a soft computing technique known as regression analysis is utilised. Regression analysis is a statistical modelling technique used to determine a mathematical relationship between dependent (target) and independent (explanatory) variables [190, 191]. In regression techniques such as polynomial regression, a model structure is first hypothesized, and then the coefficients are fit to the training data; however, symbolic regression is a distinct type of regression technique that involve both the discovery of the model structure and the coefficients within that model structure [192].

Symbolic regression is a widely used technique for the approximation of mathematical functions [193]. It explores the mathematical space to find the most desirable metamodel by a structured manner of modifying operators in a set of explicit formulae. Various formulae explored in symbolic regression can be expressed utilising a tree structure. A combinatoric optimization technique is used to obtain the best tree structure. The notable benefit of symbolic regression is its interpretability and capability to capture the underlying physics from data [194]. Symbolic regression has several advantages compared to other regression techniques, such as flexibility in the choice of operators, class of functions, and expression size. Symbolic regression to determine mathematical functions can be performed using several techniques such as genetic programming (GP) [195] and simulated annealing (SA) [196]. Although genetic programming- and simulated annealing-based symbolic regression utilize a tree structure to search for the optimal mathematical expression, the algorithmic searching methods are fundamentally different. A genetic algorithm starts with a population of possible solutions, and at each step (generation), it chooses pairs of a possible solution, joins them (crossover), and applies random changes (mutation). In contrast, simulated annealing takes a population and applies a metaheuristic function to approximate the global optimum in the large search space; this reduces the population's random variation (rate, quantity, and type). The primary advantage of simulated annealing over genetic programming is its capability to arrive at a global minimum, and other advantages include the ease of determining constants and lower relative computational cost [194]. The overall procedure utilised in this work is illustrated in Figure 14.

Simulated annealing-based symbolic regression's general idea is to have an overall

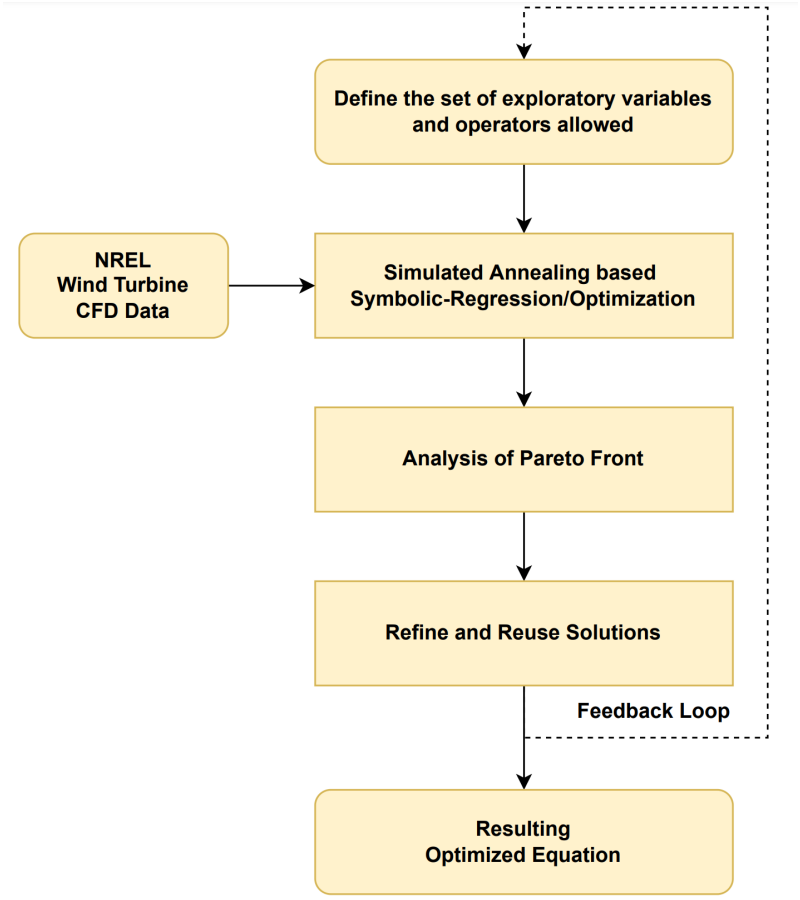

Figure 14: Flowchart of symbolic regression procedure.

look at all the components of the solution space at the start of the search, and to track one solution in the space of possible solutions. The parameters are adjusted gradually during each iteration, and the algorithm decides to either continue with the current solution or select the neighbouring solution based on probabilities (which decay over time). If the algorithm continuously accepts large adjustments during the optimization process, the starting parameters can be adjusted by reannealing. In symbolic regression, complex functions tend to fit the data better; however, complex functions are prone to over-fitting and are difficult to interpret. Therefore the objective is to determine a mathematical expression that is both simple (minimize the complexity) and fits the data (maximize the metamodel quality) using a MultiObjective Combinatorial Optimization (MOCO) method such as Pareto simulated annealing. A detailed algorithm for implementation of Pareto simulated annealing-based symbolic regression can be found in [194], and it was performed here using TuringBot python library on an AMD Ryzen 9 5900 CPU with 24 threads for about 1200 CPU hours. The authors described the limitations of machine learning-based models with training and test data derived from the findings of a single wind turbine simulation in one of their earlier publications [197]. It is advised to have data from various wind turbines in order to achieve generalizability. Since the experimental results of the NREL Phase VI wind turbine and MEXICO rotor are well acknowledged and often utilised, training data from the NREL Phase VI wind turbine and test data from the MEXICO rotor are utilised in this work.

3.6.1 Dataset

The training data were obtained from the unsteady RANS (URANS) CFD simulations of the NREL Phase VI wind turbine employing the advanced sliding mesh method from the authors' prior work [139]. Aerofoil characteristics $C_{L,3D}$ and $C_{D,3D}$ were calculated by employing Inverse BEM analysis at 18 radial positions for different inlet wind speeds of 7 m/s, 10 m/s, 15 m/s, 20 m/s, and 25 m/s.

For validation, a hold-out cross-validation strategy was considered in this study to avoid overfitting: 20 percent of the training data was held-out to perform hyper-parameter optimization. The hyper-parameters that were optimized include the coefficients of the obtained functional form.

The testing data to ensure the generalizability of the proposed model were from experimental data of the MEXICO rotor [179, 180]. The test data included the sectional aerofoil characteristics at five distinct radial positions (25 percent, 35 percent, 60 percent, 82 percent, and 92 percent) obtained at inlet wind speeds of 10 m/s, 15 m/s, and 24 m/s.

3.6.2 Model Evaluation

The model obtained from symbolic regression should fit well with the training and validation data. For this, we calculate the Root Mean Squared Error (RMSE):

$$RMSE = \sqrt{\frac{\sum_{i=1}^{N} \left(\text{Actual}Y_i - \text{Predicted}f(x_i)\right)^2}{N}} \tag{3.9}$$

If a change in model structure or model coefficients improves the obtained model (RMSE decreases), the change is accepted [194]; using this iterative process, a final model

that is compact, interpretable, and fits the training and validation data well is obtained. Other details of the training process, such as defining exploratory variables and solution search options, can be found in Section 3.7.

3.7 New Empirical Model for Stall Delay

A total of six non-dimensional exploratory variables, including the tip-speed ratio defined as ($\lambda = \Omega R/U_\infty$), the ratio of local to total radius of the wind turbine (r/R), the ratio of local chord to local radius of the wind turbine (c/r), the ratio of inflow wind to relative velocity (U_∞/U_{rel}), λ_r defined as ($\lambda_r = \Omega r/U_\infty$), and λ_{rel} defined as ($\lambda_{rel} = \Omega r/U_{rel}$), were formulated, and their values were extracted from NREL wind turbine data (see Section 3.5.1). The objective of the Pareto simulated annealing-based symbolic regression algorithm is to determine a mathematical expression to model the target variable f_L (stall delay correction parameter for lift) and f_D (stall delay correction parameter for drag) based on Equations (3.10) and 3.11, respectively.

$$f_L = f(\lambda, \frac{r}{R}, \frac{c}{r}, \frac{U_\infty}{U_{rel}}, \lambda_r, \lambda_{rel}) \tag{3.10}$$

$$f_D = g(\lambda, \frac{r}{R}, \frac{c}{r}, \frac{U_\infty}{U_{rel}}, \lambda_r, \lambda_{rel}) \tag{3.11}$$

After determining the expressions for stall delay correction parameters f_L and f_D, the three-dimensional aerodynamic coefficients ($C_{L,3D}$ and $C_{D,3D}$) can be computed from two-dimensional aerodynamic coefficients ($C_{L,2D}$ and $C_{D,2D}$) utilising Equations (3.12)

and 3.13, respectively.

$$C_{L,3D} = C_{L,2D} + f_L \left(2\pi \left(\alpha - \alpha_0\right) - C_{L,2D}\right) \tag{3.12}$$

$$C_{D,3D} = C_{D,2D} + f_D \left(C_{D,2D} - C_D(\alpha = 0)\right) \tag{3.13}$$

The six non-dimensional exploratory variables that were included to model the target stall delay correction parameters f_L and f_D are shown in Equations (3.10) and 3.11, respectively. Parameter selection (feature selection) to model the target variable using exploratory variables is performed by the algorithm automatically. This step ensures that the model is constructed only using parameters (features) that capture the underlying physics. Mathematical operators ($\times$, $\div$, exponent, and square root) were chosen for the expression search, and remaining operators such as +, $-$, and trigonometric values were excluded in order to obtain a generalised expression that is not limited to a specific range of the input parameters and to ensure that the resulting expression is not very sensitive to small changes to the input.

$$f_L = C_1 \times e^{\left(\frac{C_2}{\lambda \times \frac{c}{r}}\right)} \tag{3.14}$$

$$f_D = C_3 \times \lambda \times e^{\frac{c/r}{(C_4 \times \lambda)^\lambda}} \tag{3.15}$$

The proposed stall delay correction model determined using Pareto simulated annealing-based symbolic regression is given in Equation (3.14) and 3.15, where $C_1 = 1.425330$, $C_2 = 1.261960$, $C_3 = 0.267109$, $C_4 = 0.337107$. The choice of exploratory parameters is crucial for the symbolic regression model's capability to capture the underlying physics; therefore, the non-dimensional exploratory parameters (see Equations (3.14) and

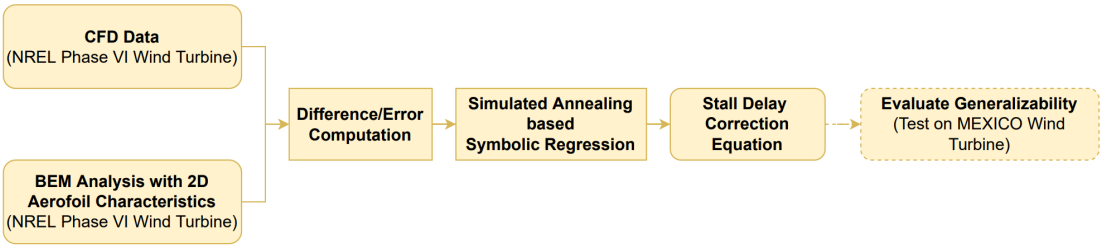

Figure 15: Flowchart describing overall workflow.

3.15) considered in this study were chosen based on extensive literature review. Further, the variables λ (tip speed ratio) and c/r (ratio of local chord to local radius) were selected automatically based on their capability to capture the underlying physics. The compact size of the expression and choice of operators in the expression reaffirms that the model is not overfit to the data. In addition, the obtained model is also validated on MEXICO rotor experimental results. The overall workflow of this study is shown in Figure 15.

3.8 Results and Discussions

This section portrays the comparative study focused on the Blade Element Momentum evaluation of the NREL Phase VI turbine and MEXICO rotor. In prior strategies for deriving corrective models, data from only one rotor were typically employed. The Lindenburg model, for instance, is based on NREL Phase VI turbine experiments. The correction computed for certain cases may not be appropriate in the other cases of different wind turbines. As a basis, the model in this study was developed using data from NREL Phase VI turbine analysis and verified using MEXICO rotor analysis. The authors Kabir and Ng [139] executed earlier CFD assessments of the NREL Phase VI turbine and computed $C_{L,3D}$ and $C_{D,3D}$ values using an enhanced Inverse BEM method because the aerofoil

coefficients from experiments were not directly available. Kabir and Ng [139] verified their forecasts with other previous works [198–202] at five radial positions (30 percent, 47 percent, 63 percent, 80 percent, and 95 percent). Therefore, if the prediction at five radial positions is accurate, the values predicted at other radial positions (13 positions used for the design) would be accurate as well. In contrast to earlier models, which only use data from the five radial positions specified in the experimental details, additional radial positions were utilised for data creation in order to obtain a more accurate corrective model. In this comparison, 2D aerofoil characteristics of an S809 aerofoil from Delft University of Technology (DUT) wind tunnel analysis for Reynolds numbers of 1×10^6 up to 20.6° AoA were used, and the Viterna and Corrigon method [203] for polar extrapolation was used, as described by Kabir and Ng [139]. Since the MEXICO rotor was deployed for validation, the sectional aerofoil characteristics at five distinct radial positions (25 percent, 35 percent, 60 percent, 82 percent, and 92 percent) were calculated from the experimental results using the Inverse BEM method executed in MATLAB. In this comparative investigation, BEM results without and with correction models for stall delay are compared to 3D aerofoil coefficients of the NREL Phase VI turbine, followed by validation with MEXICO rotor results.

3.8.1 3D Aerodynamic Characteristics

3.8.1.1 Angle of Attack Distribution

Figure 16 depicts the distribution of angles of attack over the blade length for wind speeds ranging from 7 to 25 m/s, as calculated from the BEM assessment of the NREL Phase VI turbine without and with distinct correction models for stall delay. Figure

17 presents a comparison of the distribution of angles of attack over the blade length for the MEXICO rotor at wind speeds of 10 m/s, 15 m/s, and 24 m/s. It is essential to realise that whereas correction models for stall delay alter anticipated forces on the blades, the influence on distribution of angles of attack is minimal. The sole exception is when the correction models for stall delay predict very high load variations in the area of the root. In these cases, a comparable local variation in angles of attack is created at the root, as predicted by BEM analysis with correction models for stall delay, which are close to 3D values predicted by Inverse BEM analyses, but BEM with no correction models overestimates angles of attack.

3.8.1.2 Comparison of C_L Prediction throughout the Blade Length

Figure 18 illustrates the contrast of the estimated C_L value throughout the blade length by the BEM assessment without and with the different existing correction models for stall delay and the model proposed with the $C_{L,3D}$ value obtained from the CFD analyses of the NREL Phase VI turbine for wind speeds of 7 m/s, 10 m/s, 15 m/s, 20 m/s, and 25 m/s. BEM predicts the enhancement in lift coefficient attributable to stall delay quite decently up to a wind speed of 10 m/s with all correction models for stall delay [139]. With increasing wind speed, BEM with previous correction models for stall delay, such as the Dumitrescu and Cardos model [174–176], estimate higher C_L values in comparison to $C_{L,3D}$ calculation from the CFD study for the NREL Phase VI turbine [139]. The Lindenburg model [144] substantially overpredicts at extremely high wind speed of 25 m/s, as predicted earlier by Breton et al. [146] and Kabir and Ng [139]; however, for other wind speeds, the trajectory of increase in C_L throughout the blade length is close to the $C_{L,3D}$

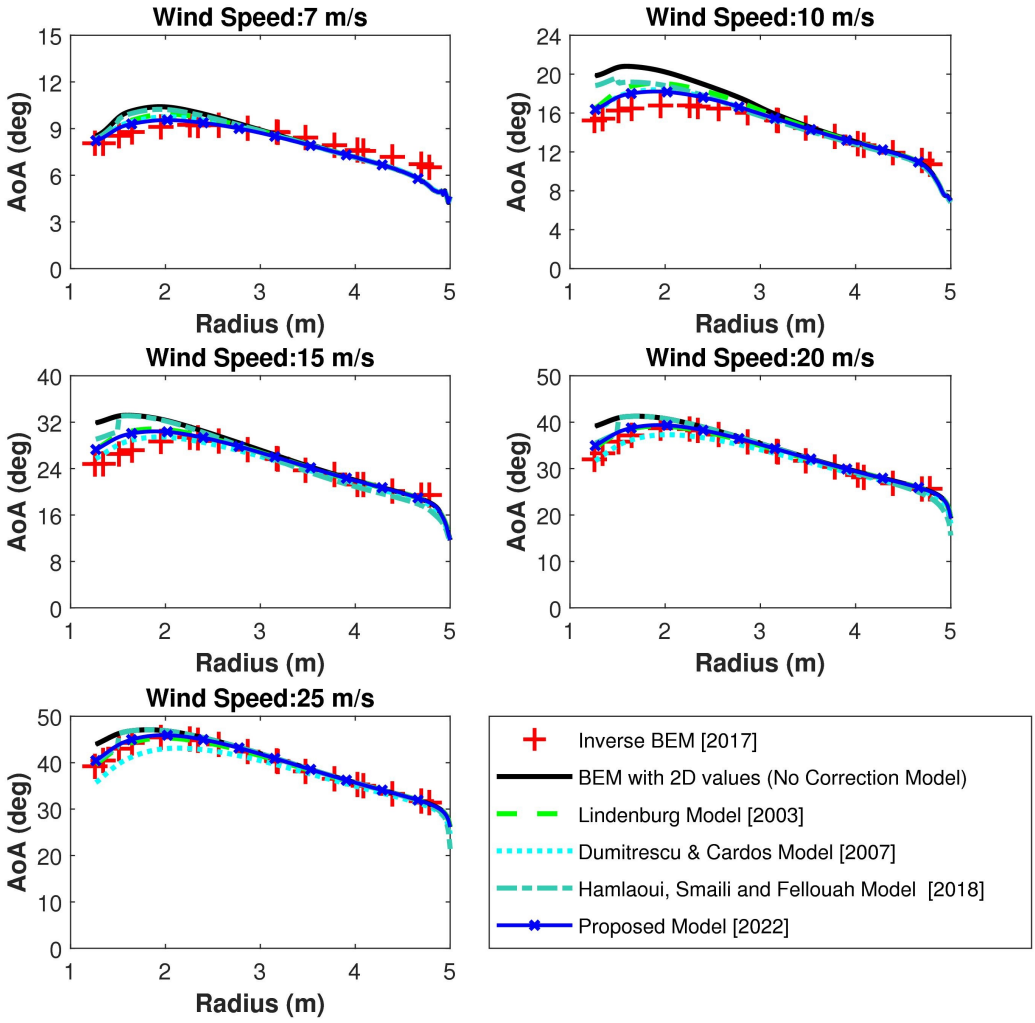

Figure 16: Contrast of evaluated AoA throughout the blade length from BEM analysis without and with different correction models for stall delay and Inverse BEM method for NREL Phase VI turbine.

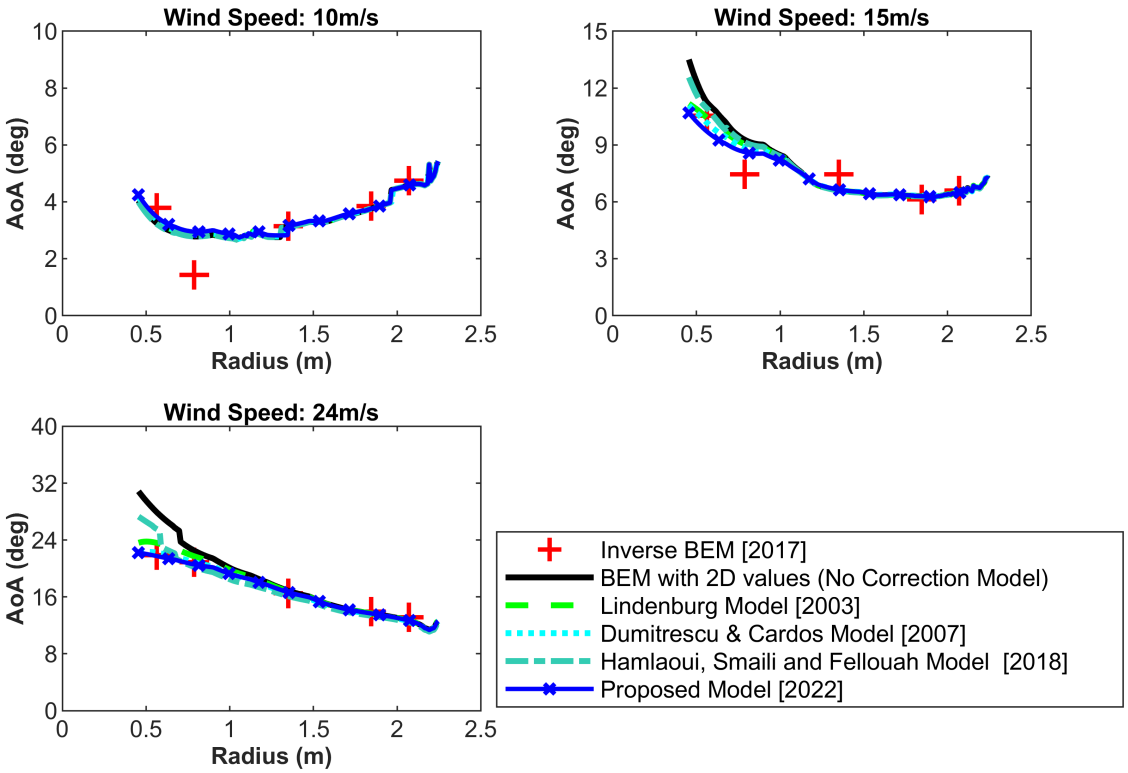

Figure 17: Contrast of evaluated AoAs throughout the blade length from BEM analysis without and with different correction models for stall delay and Inverse BEM method for MEXICO rotor.

throughout the blade length. The Hamlaoui, Smaili and Fellouah model [177] for r/R <30 percent, which is considered to be the lower inboard region of the blade, and for r/R $>$ 50 percent, which is considered to be the top half of the blade, gives predictions comparable to the 3D values. However, the value of C_L shows a profound downward trend for r/R between 30 percent and 50 percent, ignoring the effect of stall delay. The root cause of this tendency is that Hamlaoui et al. [177] employed values from only five radial positions: 30 percent, 47 percent, 63 percent, 80 percent, and 95 percent. It is worth noting that just around 30 percent of the r/R is located in the inboard portion, where the effect of stall delay is strongest, whereas the other four radial positions are almost on the blade's upper half. As a consequence, they incorporated two components in their correction models: r/R $<$ 30 percent and r/R $>$ 30 percent. However, because the second component is based on values predicted above 47 percent, this model fails to estimate the effect of stall delay between 30 and 47 percent. As a corollary, 3D values computed at additional radial positions (0.250R, 0.267R, 0.328R, 0.390R, 0.450R, 0.510R, 0.570R, 0.633R, 0.691R, and 0.750R) were also included in estimating the correction models in our work. Therefore, for all wind speeds, the current proposed model determines results close to the $C_{L,3D}$ for the NREL Phase VI turbine. The accuracy of the proposed model is confirmed by computing the error percentage at four radial positions (0.30R, 0.47R, 0.63R, and 0.80R) considered in the experimental analysis and is presented in Figure 19. As recognised, the percentage of error calculated from the proposed method is predominantly less compared to the other models. The proposed model can only be used up to 0.8R, whereas the calculated values of C_L at r/R $>$ 80 percent are $C_{L,2D}$ values without any added correction. Unlike the inboard

section, $C_{L,3D}$ in the tip region is lower than $C_{L,2D}$. This is due to tip vortices with the secondary flow generated at the tip [140, 146]. The current model is only meant to take into account stall delay; therefore, the correction model is only proposed up to 0.8 R. For this reason, radial positions smaller than 0.8 R are represented in the error comparison for both the NREL Phase VI and MEXICO rotors. In the future, a new model will be proposed to account for the correction in the reduction of the lift coefficient due to the effect of tip vortices. Figure 20 depicts the C_L distribution estimated from BEM analysis without and with correction models for stall delay along the MEXICO rotor's blade length for three distinct wind speeds. Figure 21 shows the error comparison for C_L prediction at three distinct radial positions (0.25R, 0.35R, and 0.60R) utilised in the experimental analysis, ignoring radial positions above 0.8R. Almost all models forecast closure values with the experimental data at wind speeds of 10 m/s and 15 m/s; however, at 24 m/s, the Dumitrescu and Cardos [174–176] model and the proposed model are quite similar to 3D values obtained from the experimental data, while the Lindenburg model [144] is slightly lower but follows the same trend. The Hamlaoui, Smaili and Fellouah model [177], on the other hand, is a total catastrophe. As per Figures 20 and 21, the proposed model outperforms the existing correction models for stall delay.

3.8.1.3 Comparison of C_D Prediction throughout the Blade Length

Figure 22 compares the estimated C_D value throughout the blade length using BEM without or with the correction models for stall delay using the $C_{D,3D}$ values obtained through the Inverse BEM method of CFD analysis at wind speeds of 7 m/s, 10 m/s, 15 m/s, 20 m/s, and 25 m/s for the NREL Phase VI turbine. The BEM utilising earlier correction

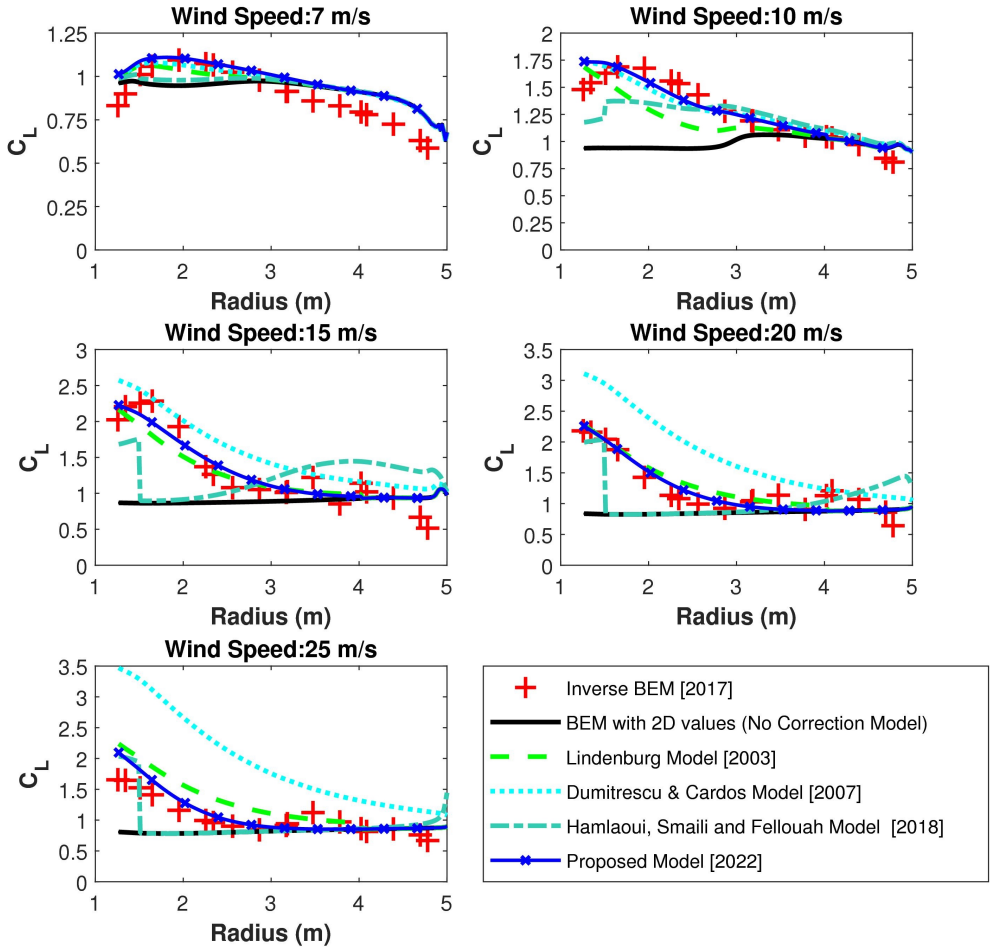

Figure 18: Contrast of evaluated C_L throughout the blade length from BEM analysis without and with different correction models for stall delay and Inverse BEM method for NREL Phase VI turbine.

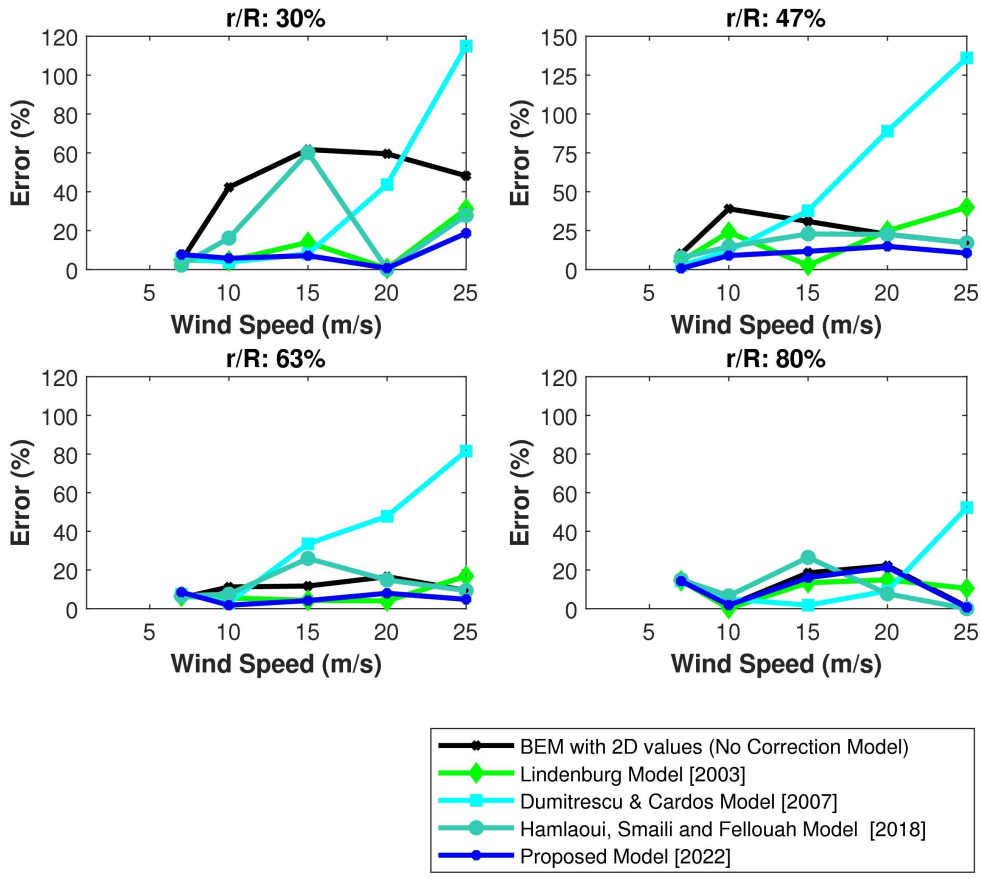

Figure 19: Error in C_L computation by each model at different radial positions with different wind speeds for NREL Phase VI turbine.

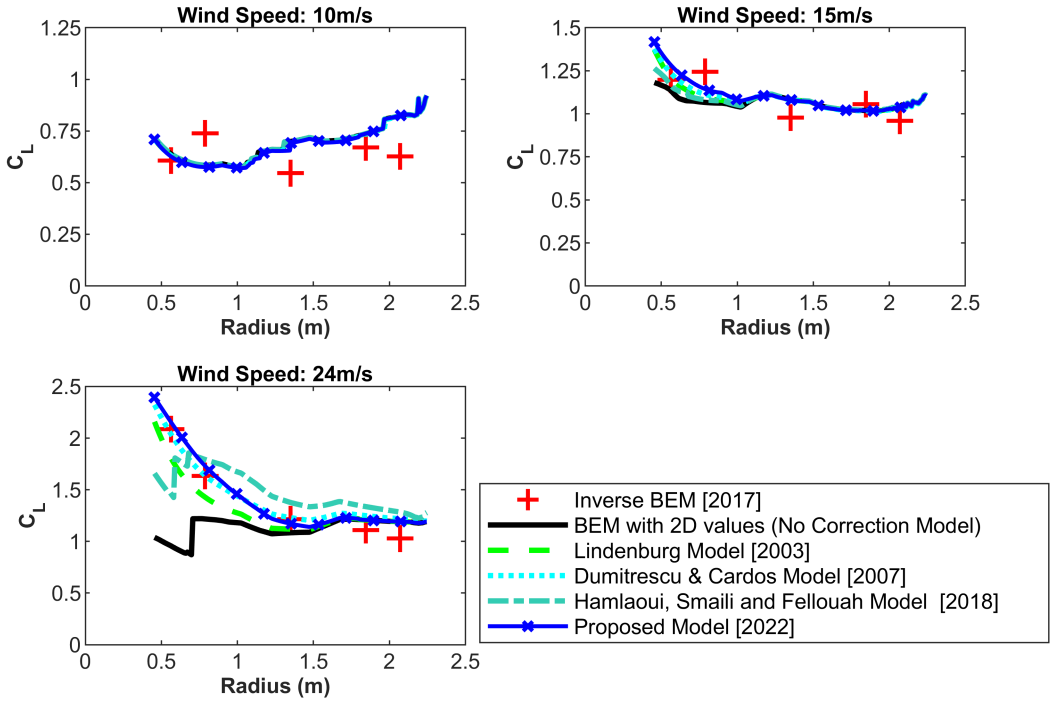

Figure 20: Contrast of evaluated C_L throughout the blade length from BEM analysis without and with different correction models for stall delay and Inverse BEM method for MEXICO rotor.

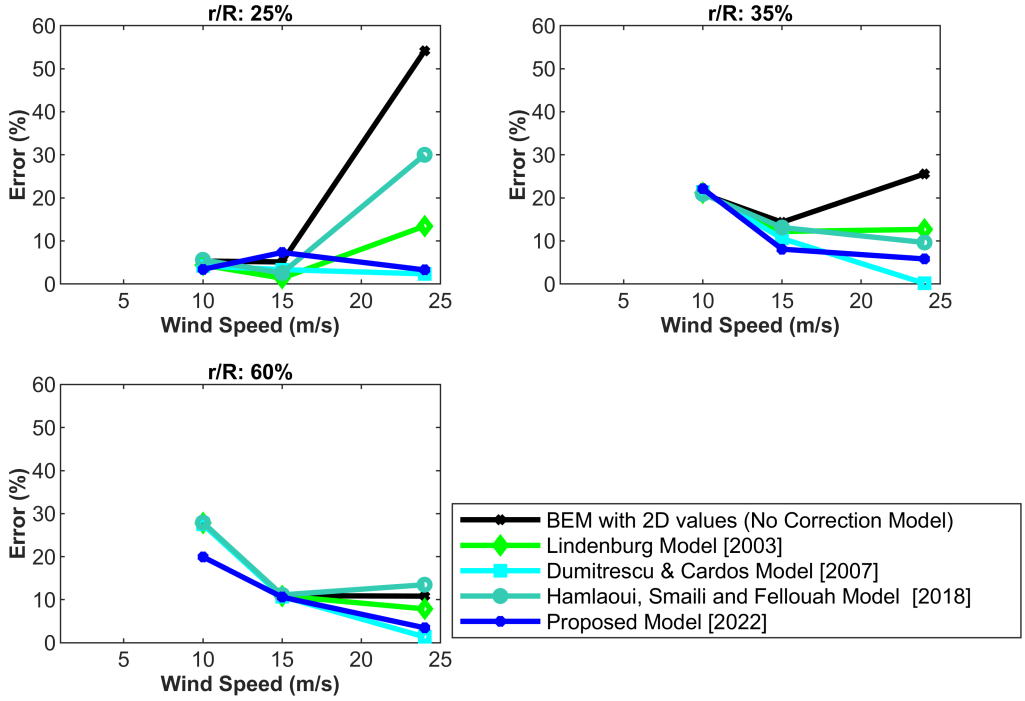

Figure 21: Error in C_L computation by each model at different radial positions with different wind speeds for MEXICO rotor.

models for stall delay predicts lower C_D values than the $C_{D,3D}$ determined from CFD analysis using the Inverse BEM approach. The values estimated based on earlier correction models for stall delay considered for comparison in this study are close to the $C_{D,2D}$ values since these models do not account for drag coefficient corrections. On the contrary, since there was a divergence noticed in $C_{D,3D}$ and $C_{D,2D}$ for all wind speeds, a new model is proposed and compared in Figure 22. While previous models did not even approach the 3D values, the proposed model predicts extremely close at high wind speeds (15 m/s, 20 m/s, and 25 m/s) and relatively close at low wind speeds (7 m/s and 10 m/s). Figure 22 compares the estimated C_D value throughout the blade length using BEM without or with the correction models for stall delay with $C_{D,3D}$ values obtained through the Inverse BEM method of CFD analysis on wind speeds of 10 m/s, 15 m/s, and 24 m/s for the MEXICO rotor. Figures 22 and 23 show that for the NREL Phase VI turbine, $C_{D,3D}$ is often higher than $C_{D,2D}$, indicating that rotational effects were associated with a notable drag rise, but for the MEXICO rotor, rotational effects were associated with a small drag drop. Ivan Harreaz [140] exploited OpenFOAM to do CFD simulations of the MEXICO rotor and calculated sectional $C_{L,3D}$ and $C_{D,3D}$ at three distinct wind speeds. Ivan Harreaz [140] also noticed a similar discrepancy in C_D predictions. Other drag correction models, such as those by Chaviaropolous and Hansen [169] and Raj [170], anticipate an increase in C_D, but the Corrigan and Schillings [171] and Du and Selig [173, 204] models predict a decrease in C_D. Other models, such as those by Snel [168], Lindenburg [144], Dumitrescu and Cardos [174–176], and Hamlaoui , Smaili and Fellouah [177], have not proposed models or taken into account a C_D discrepancy. In fact, it can be noticed from Figure 23 that there

is no discernible difference between the $C_{D,3D}$ and $C_{D,2D}$ values for the MEXICO rotor. Furthermore, according to Ivan Harreaz [140], rotational effects have minimal influence on C_D (except at r/R = 60 percent). Guntur et al. [150], who used the MEXICO rotor to evaluate correction models, came to the conclusion that C_D correction may not be essential. Ivan Harreaz [140] concluded that the effect of rotation on drag appears to be aerofoil-type dependant, which we concur with. Since, as stated in Section 3.1 of this paper, the main concern of this work is to predict lift enhancement due to stall delay. Further, the effect of rotation on drag is minimal compared to its effect on lift, and because this work employs a novel dimension of using Machine Learning (ML), we propose a preliminary model for drag correction depending on the predictions of the NREL Phase VI turbine. Despite the fact that this model is dependent on NREL Phase VI turbine data, the forecast for the MEXICO rotor is still close. In the future, an additional relevant parameter representing aerofoil type will be taken into account, and a new model for drag correction with greater accuracy will be built that enables forecasting of both increases and decreases in the drag coefficient based on aerofoil type.

3.9 Conclusions and Future Works

Practically, direct CFD analyses of wind farms with a significant number of wind turbines are not feasible. Hence in CFD analyses of wind farms, indirect rotor modelling, such as Actuator Disk (AD), Actuator Line (AL), and Actuator Surface (AS) modelling, are necessary. This indirect rotor modelling depends on BEM analyses for aerodynamic phenomena performance. Hence, if the prediction of BEM is wrong, that leads to incorrect CFD analyses. Therefore, accurate prediction from BEM is essential for the CFD analyses

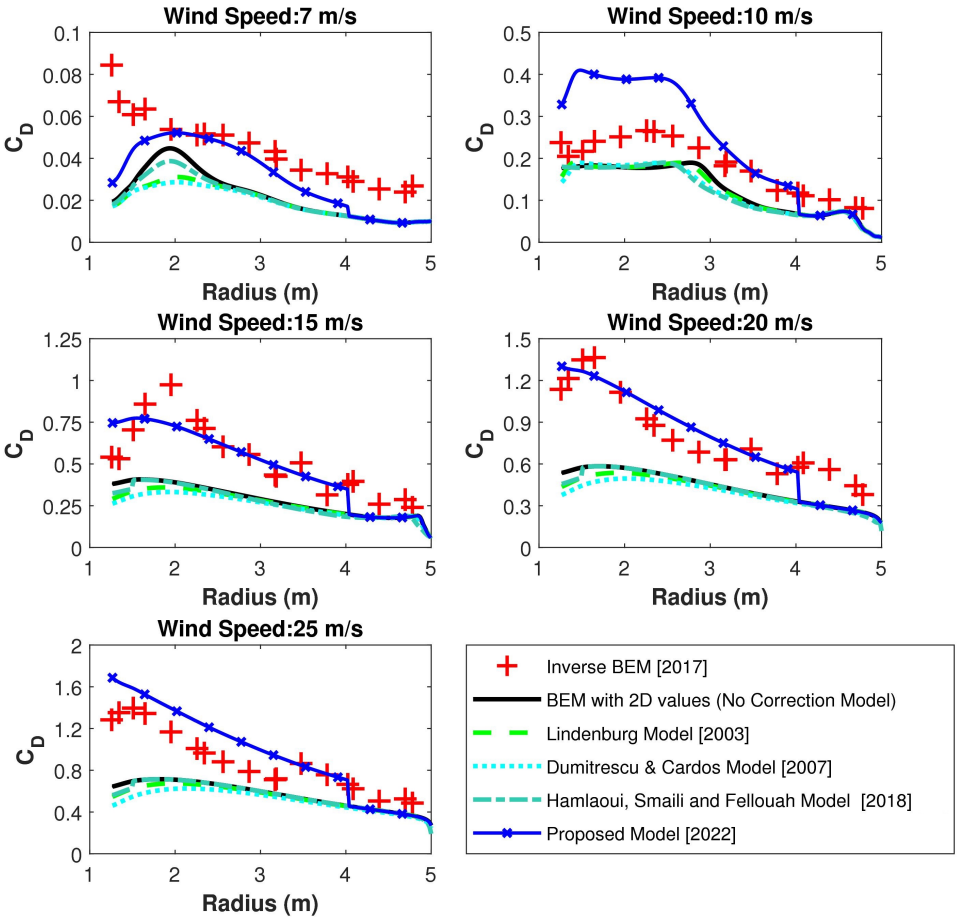

Figure 22: Contrast of evaluated C_D throughout the blade length from BEM analysis without and with different correction models for stall delay and Inverse BEM method for NREL Phase VI turbine.

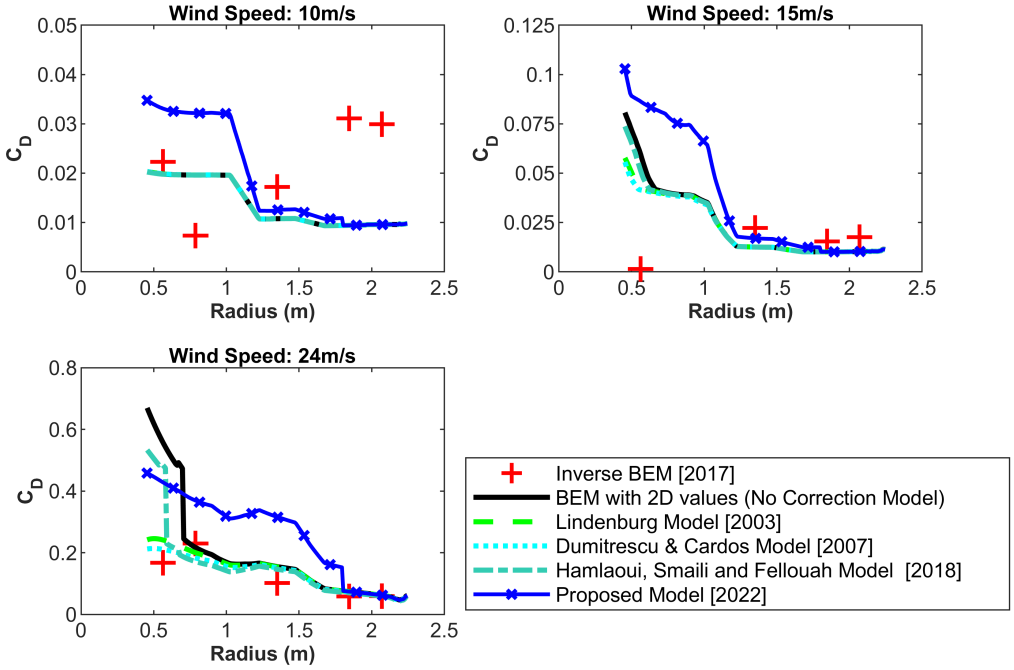

Figure 23: Contrast of evaluated C_D throughout the blade length from BEM analysis without and with different correction models for stall delay and Inverse BEM method for MEXICO rotor.

of a wind farm. This work, thus, takes account of an attempt to improve the precision of BEM in the prediction of aerodynamic loads. In this investigation, a new correction model was derived using soft computing called Symbolic Regression based on the disparity between 3D CFD observations and 2D values of aerofoil coefficients throughout the blade length for different wind speeds of the NREL Phase VI turbine. It has been noted from the literature that correction models for stall delay derived from conventional hard computing techniques are not accurate enough. Contrarily, BEM predicts the lift and drag coefficient closure of the CFD results while using the new correction model for stall delay for the NREL Phase VI turbine [139]. The proposed model is validated using 3D aerofoil characteristics collected from the MEXICO rotor experimental results with an Inverse BEM approach. The proposed model effectively predicts closure for lift coefficient comparisons, but the drag coefficients are slightly over-predicted. This might be due to the effect of rotation on drag, which differs based on aerofoil type. The drag coefficient increases with rotation for the NREL Phase VI turbine but decreases for the MEXICO rotor. This research focuses on the rise in lift coefficients caused by stall delay at the inboard sections; therefore, significant emphasis is placed on lift coefficient correction models. A preliminary model for the drag coefficient is also suggested and found to be adequate. The proposed model for lift correction is good for r/R $<$ 80 percent because at r/R $>$ 80 percent, 3D lift coefficients are lower than 2D lift coefficients due to the influence of tip vortices; we are now developing a new model to compute the decrease in lift coefficients at the blade's tip. In addition, we are focusing on a novel correction model for drag coefficients based on the type of aerofoil.

Ongoing research seeks to improve rotor and wake aerodynamic prediction in wind farm modelling and optimization. The authors focused on wake aerodynamics in their earlier works [136, 205, 206] and derived empiric relationships specifically to determine the wake velocity and turbulence intensity. In this article, the authors emphasised one of the unsteady effects in rotor aerodynamics modelling called stall delay to accurately model three-dimensional rotational augmentation effect. In the future, ML-based models will be developed for other unsteady 3D effects such as dynamic stall [207–209], dynamic inflow [210], yaw misalignment [211], wind shear [212], and tower shadow [207] to improve rotor modelling techniques. Subsequently, both these rotor and wake aerodynamic modelling strategies can be utilised to extract data to optimize axial flow wind farms to estimate the power from a given landscape.

CHAPTER 4

CONCLUSION

In conclusion, ”Machine Learning-based Predictive Modeling of Stochastic Systems” is a critical and active area of research with the potential to significantly contribute to various fields. This dissertation aimed to develop machine learning-based methods for early glaucoma detection using electroretinography signals and predicting stall delay in wind turbines. Through the development and evaluation of these models, it was demonstrated that machine learning can accurately detect various stages of glaucoma from ERG signals and predict stall delay in wind turbines. The research also emphasized the need for model interpretability and generalizability to perform well on unseen data. Moreover, the results suggest that the proposed method could be beneficial in real-world applications, improving disease management and enhancing the efficiency and performance of wind turbine systems. Overall, this dissertation showcases the potential of machine learning-based predictive modeling of stochastic systems and suggests that further research in this area could lead to significant improvements in various fields.

The results obtained in this study strongly indicate that the employed methods can consistently identify dominant features for classification and regression from STR, Oscillatory Potentials (OPs), and other ERG tests. This is in line with previous work on the sensitivity of OPs and flicker to subtle changes in RGC function and viability. Additionally, our approach identified novel dominant distinguishing features, such as Shannon Entropy Values for Maximal Overlap Discrete Wavelet Packet Transform (MOD-PWT) and AR

coefficients, which were not distinguishable by traditional methods. This highlights the potential of the current machine-learning-based algorithm in detecting subtle changes in ERG signals corresponding to different stages of glaucoma disease development. This capability could serve as a foundational step for creating a reliable framework for early glaucoma detection and monitoring the efficacy of therapeutic interventions in both clinical practice and novel drug development.

Practical implementation of direct CFD analyses for wind farms with numerous wind turbines is not feasible. Therefore, indirect rotor modeling, such as Actuator Disk (AD), Actuator Line (AL), and Actuator Surface (AS) modeling, are necessary and depend on BEM analyses for aerodynamic performance. Accurate BEM predictions are essential for the CFD analyses of a wind farm. This work aimed to improve BEM's precision in predicting aerodynamic loads by deriving a new correction model using soft computing called Symbolic Regression based on the disparity between 3D CFD observations and 2D values of airfoil coefficients throughout the blade length for different wind speeds of the NREL Phase VI turbine. The proposed model effectively predicts closure for lift coefficient comparisons, but the drag coefficients are slightly over-predicted. A preliminary model for the drag coefficient is also suggested and found to be adequate. The focus is now on developing a new model to compute the decrease in lift coefficients at the blade's tip and a novel correction model for drag coefficients based on the type of airfoil.

Bibliography

[1] G. Ronsten, "Static pressure measurements on a rotating and a non-rotating 2.375 m wind turbine blade. comparison with 2d calculations," *Journal of Wind Engineering and Industrial Aerodynamics*, vol. 39, no. 1-3, pp. 105–118, 1992.

[2] R. Pereira, "Validating the beddoes-leishman dynamic stall model in the horizontal axis wind turbine environment," Master's thesis, Department of Control and Operations, Delft University of Technology, Delft, The Netherlands, 2010.

[3] C. Lindenburg, "Modelling of rotational augmentation based on engineering considerations and measurements," in *European Wind Energy Conference, London*, 2004, pp. 22–25.

[4] I. I. Bussel, G. Wollstein, and J. S. Schuman, "Oct for glaucoma diagnosis, screening and detection of glaucoma progression," *British Journal of Ophthalmology*, vol. 98, no. Suppl 2, pp. ii15–ii19, 2014.

[5] B. M. Fidalgo, D. P. Crabb, and J. G. Lawrenson, "Methodology and reporting of diagnostic accuracy studies of automated perimetry in glaucoma: evaluation using a standardised approach," *Ophthalmic and Physiological Optics*, vol. 35, no. 3, pp. 315–323, 2015.

[6] P. J. Ernest, J. S. Schouten, H. J. Beckers, F. Hendrikse, M. H. Prins, and C. A. Webers, "The evidence base to select a method for assessing glaucomatous visual field progression," *Acta ophthalmologica*, vol. 90, no. 2, pp. 101–108, 2012.

[7] O. Saeedi, M. V. Boland, L. D'Acunto, R. Swamy, V. Hegde, S. Gupta, A. Venjara, J. Tsai, J. S. Myers, S. R. Wellik *et al.*, "Development and comparison of machine learning algorithms to determine visual field progression," *Translational Vision Science & Technology*, vol. 10, no. 7, pp. 27–27, 2021.

[8] A. V. Turalba and C. Grosskreutz, "A review of current technology used in evaluating visual function in glaucoma," in *Seminars in ophthalmology*, vol. 25, no. 5-6. Taylor & Francis, 2010, pp. 309–316.

[9] A. Lee, P. Taylor, J. Kalpathy-Cramer, and A. Tufail, "Machine learning has arrived!" *Ophthalmology*, vol. 124, no. 12, pp. 1726–1728, 2017.

[10] D. A. Sim, P. A. Keane, A. Tufail, C. A. Egan, L. P. Aiello, and P. S. Silva, "Automated retinal image analysis for diabetic retinopathy in telemedicine," *Current diabetes reports*, vol. 15, no. 3, p. 14, 2015.

[11] H. Zhu, A. Poostchi, S. A. Vernon, and D. P. Crabb, "Detecting abnormality in optic nerve head images using a feature extraction analysis," *Biomedical optics express*, vol. 5, no. 7, pp. 2215–2230, 2014.

[12] R. Asaoka, H. Murata, A. Iwase, and M. Araie, "Detecting preperimetric glaucoma with standard automated perimetry using a deep learning classifier," *Ophthalmology*, vol. 123, no. 9, pp. 1974–1980, 2016.

[13] G. An, K. Omodaka, K. Hashimoto, S. Tsuda, Y. Shiga, N. Takada, T. Kikawa, H. Yokota, M. Akiba, and T. Nakazawa, "Glaucoma diagnosis with machine learning based on optical coherence tomography and color fundus images," *Journal of healthcare engineering*, vol. 2019, 2019.

[14] L. M. Brandao, M. Monhart, A. Schötzau, A. A. Ledolter, and A. M. Palmowski-Wolfe, "Wavelet decomposition analysis in the two-flash multifocal erg in early glaucoma: a comparison to ganglion cell analysis and visual field," *Documenta Ophthalmologica*, vol. 135, no. 1, pp. 29–42, 2017.

[15] A. A. Ledolter, M. Monhart, A. Schoetzau, M. G. Todorova, and A. M. Palmowski-Wolfe, "Structural and functional changes in glaucoma: comparing the two-flash multifocal electroretinogram to optical coherence tomography and visual fields," *Documenta Ophthalmologica*, vol. 130, no. 3, pp. 197–209, 2015.

[16] R. S. Harwerth, M. Crawford, L. J. Frishman, S. Viswanathan, E. L. Smith Iii, and L. Carter-Dawson, "Visual field defects and neural losses from experimental glaucoma," *Progress in retinal and eye research*, vol. 21, no. 1, pp. 91–125, 2002.

[17] B. Fortune, L. Wang, B. V. Bui, G. Cull, J. Dong, and G. A. Cioffi, "Local ganglion cell contributions to the macaque electroretinogram revealed by experimental nerve

fiber layer bundle defect," *Investigative ophthalmology & visual science*, vol. 44, no. 10, pp. 4567–4579, 2003.

[18] S. T. Takagi, Y. Kita, F. Yagi, and G. Tomita, "Macular retinal ganglion cell complex damage in the apparently normal visual field of glaucomatous eyes with hemifield defects," *Journal of glaucoma*, vol. 21, no. 5, pp. 318–325, 2012.

[19] Y. H. Aldebasi, N. Drasdo, J. E. Morgan, and R. V. North, "S-cone, l+ m-cone, and pattern, electroretinograms in ocular hypertension and glaucoma," *Vision research*, vol. 44, no. 24, pp. 2749–2756, 2004.

[20] L. M. Ventura and V. Porciatti, "Pattern electroretinogram in glaucoma," *Current Opinion in Ophthalmology*, vol. 17, no. 2, pp. 196–202, 2006.

[21] M. C. Leske, A. Heijl, L. Hyman, B. Bengtsson, L. Dong, Z. Yang, E. Group *et al.*, "Predictors of long-term progression in the early manifest glaucoma trial," *Ophthalmology*, vol. 114, no. 11, pp. 1965–1972, 2007.

[22] P. Palmberg, "Answers from the ocular hypertension treatment study," *Archives of ophthalmology*, vol. 120, no. 6, pp. 829–830, 2002.

[23] L. J. Rohowetz, J. G. Kraus, and P. Koulen, "Reactive oxygen species-mediated damage of retinal neurons: Drug development targets for therapies of chronic neurodegeneration of the retina," *International journal of molecular sciences*, vol. 19, no. 11, p. 3362, 2018.

[24] J. Tang, F. Hui, X. Hadoux, B. Soares, M. Jamieson, P. van Wijngaarden, M. Coote, and J. G. Crowston, "Short-term changes in the photopic negative response following intraocular pressure lowering in glaucoma," *Investigative Ophthalmology & Visual Science*, vol. 61, no. 10, pp. 16–16, 2020.

[25] F. Hui, J. Tang, P. A. Williams, M. B. McGuinness, X. Hadoux, R. J. Casson, M. Coote, I. A. Trounce, K. R. Martin, P. van Wijngaarden *et al.*, "Improvement in inner retinal function in glaucoma with nicotinamide (vitamin b3) supplementation: A crossover randomized clinical trial," *Clinical & experimental ophthalmology*, vol. 48, no. 7, pp. 903–914, 2020.

[26] I. Kononenko, "Machine learning for medical diagnosis: history, state of the art and perspective," *Artificial Intelligence in medicine*, vol. 23, no. 1, pp. 89–109, 2001.

[27] P. J. Lisboa, "A review of evidence of health benefit from artificial neural networks in medical intervention," *Neural networks*, vol. 15, no. 1, pp. 11–39, 2002.

[28] J. McPadden, T. J. Durant, D. R. Bunch, A. Coppi, N. Price, K. Rodgerson, C. J. Torre Jr, W. Byron, A. L. Hsiao, H. M. Krumholz *et al.*, "Health care and precision medicine research: analysis of a scalable data science platform," *Journal of medical Internet research*, vol. 21, no. 4, p. e13043, 2019.

[29] C. H. Lee and H.-J. Yoon, "Medical big data: promise and challenges," *Kidney research and clinical practice*, vol. 36, no. 1, p. 3, 2017.

[30] A. Y. Hannun, P. Rajpurkar, M. Haghpanahi, G. H. Tison, C. Bourn, M. P. Turakhia, and A. Y. Ng, "Cardiologist-level arrhythmia detection and classification in ambulatory electrocardiograms using a deep neural network," *Nature medicine*, vol. 25, no. 1, pp. 65–69, 2019.

[31] A. Holzinger, "Trends in interactive knowledge discovery for personalized medicine: cognitive science meets machine learning," *The IEEE intelligent informatics bulletin*, vol. 15, no. 1, pp. 6–14, 2014.

[32] S. J. AlâAref, K. Anchouche, G. Singh, P. J. Slomka, K. K. Kolli, A. Kumar, M. Pandey, G. Maliakal, A. R. Van Rosendael, A. N. Beecy *et al.*, "Clinical applications of machine learning in cardiovascular disease and its relevance to cardiac imaging," *European heart journal*, vol. 40, no. 24, pp. 1975–1986, 2019.

[33] J. A. Cruz and D. S. Wishart, "Applications of machine learning in cancer prediction and prognosis," *Cancer informatics*, vol. 2, p. 117693510600200030, 2006.

[34] H. Liu, X. Ji, S. Dhaliwal, S. N. Rahman, M. McFarlane, A. Tumber, J. Locke, T. Wright, A. Vincent, and C. Westall, "Evaluation of light-and dark-adapted ergs using a mydriasis-free, portable system: clinical classifications and normative data," *Documenta Ophthalmologica*, vol. 137, no. 3, pp. 169–181, 2018.

[35] K. Asakawa, K. Amino, M. Iwase, Y. Kusayanagi, A. Nakamura, R. Suzuki, T. Yuuki, and H. Ishikawa, "New mydriasis-free electroretinogram recorded with skin electrodes in healthy subjects," *BioMed research international*, vol. 2017, 2017.

[36] K. Kato, M. Kondo, R. Nagashima, A. Sugawara, M. Sugimoto, H. Matsubara, D. L. McCulloch, and K. Ikesugi, "Factors affecting mydriasis-free flicker ergs recorded with real-time correction for retinal illuminance: study of 150 young healthy subjects," *Investigative ophthalmology & visual science*, vol. 58, no. 12, pp. 5280–5286, 2017.

[37] A. E. Hobby, D. Kozareva, E. Yonova-Doing, I. T. Hossain, M. Katta, B. Huntjens, C. J. Hammond, A. M. Binns, and O. A. Mahroo, "Effect of varying skin surface electrode position on electroretinogram responses recorded using a handheld stimulating and recording system," *Documenta Ophthalmologica*, vol. 137, no. 2, pp. 79–86, 2018.

[38] N. Nakamura, K. Fujinami, Y. Mizuno, T. Noda, and K. Tsunoda, "Evaluation of cone function by a handheld non-mydriatic flicker electroretinogram device," *Clinical Ophthalmology (Auckland, NZ)*, vol. 10, p. 1175, 2016.

[39] T. T. Man, Y. W. Yip, F. K. Cheung, W. S. Lee, C. P. Pang, and M. E. Brelén, "Evaluation of electrical performance and properties of electroretinography electrodes," *Translational vision science & technology*, vol. 9, no. 7, pp. 45–45, 2020.

[40] M. I. Jordan and T. M. Mitchell, "Machine learning: Trends, perspectives, and prospects," *Science*, vol. 349, no. 6245, pp. 255–260, 2015.

[41] S. Shi, Q. Wang, P. Xu, and X. Chu, "Benchmarking state-of-the-art deep learning software tools," in *2016 7th International Conference on Cloud Computing and Big Data (CCBD)*. IEEE, 2016, pp. 99–104.

[42] T. B. Trafalis and H. Ince, "Support vector machine for regression and applications to financial forecasting," in *Proceedings of the IEEE-INNS-ENNS International Joint Conference on Neural Networks. IJCNN 2000. Neural Computing: New Challenges and Perspectives for the New Millennium*, vol. 6. IEEE, 2000, pp. 348–353.

[43] H. Omrani, "Predicting travel mode of individuals by machine learning," *Transportation Research Procedia*, vol. 10, pp. 840–849, 2015.

[44] M. A. Ahmad, C. Eckert, and A. Teredesai, "Interpretable machine learning in healthcare," in *Proceedings of the 2018 ACM international conference on bioinformatics, computational biology, and health informatics*, 2018, pp. 559–560.

[45] K. Shailaja, B. Seetharamulu, and M. Jabbar, "Machine learning in healthcare: A review," in *2018 Second international conference on electronics, communication and aerospace technology (ICECA)*. IEEE, 2018, pp. 910–914.

[46] M. Z. Khan, M. K. Gajendran, Y. Lee, and M. A. Khan, "Deep neural architectures for medical image semantic segmentation," *IEEE Access*, 2021.

[47] A. Saxe, S. Nelli, and C. Summerfield, "If deep learning is the answer, what is the question?" *Nature Reviews Neuroscience*, vol. 22, no. 1, pp. 55–67, 2021.

[48] D. C. Hood, V. C. Greenstein, K. Holopigian, R. Bauer, B. Firoz, J. M. Liebmann, J. G. Odel, and R. Ritch, "An attempt to detect glaucomatous damage to the inner retina with the multifocal erg," *Investigative ophthalmology & visual science*, vol. 41, no. 6, pp. 1570–1579, 2000.

[49] A. A. Ledolter, S. A. Kramer, M. G. Todorova, A. Schötzau, and A. M. Palmowski-Wolfe, "The effect of filtering on the two-global-flash mferg: identifying the optimal range of frequency for detecting glaucomatous retinal dysfunction," *Documenta Ophthalmologica*, vol. 126, no. 2, pp. 117–123, 2013.

[50] X. Luo, N. B. Patel, R. S. Harwerth, and L. J. Frishman, "Loss of the low-frequency component of the global-flash multifocal electroretinogram in primate eyes with experimental glaucoma," *Investigative ophthalmology & visual science*, vol. 52, no. 6, pp. 3792–3804, 2011.

[51] J. Miguel-Jiménez, L. Boquete, S. Ortega, J. Rodriguez-Ascariz, and R. Blanco, "Glaucoma detection by wavelet-based analysis of the global flash multifocal electroretinogram," *Medical engineering & physics*, vol. 32, no. 6, pp. 617–622, 2010.

[52] A. Palmowski-Wolfe, M. Todorova, and S. Orgül, "Multifocal oscillatory potentials in the âtwo global flashâmferg in high and normal tension primary open-angle glaucoma," *J Clin Exp Ophthalmol*, vol. 2, p. 167, 2011.

[53] B. Fortune, M. A. Bearse, G. A. Cioffi, and C. A. Johnson, "Selective loss of an oscillatory component from temporal retinal multifocal erg responses in glaucoma," *Investigative ophthalmology & visual science*, vol. 43, no. 8, pp. 2638–2647, 2002.

[54] P. Thienprasiddhi, V. C. Greenstein, C. S. Chen, J. M. Liebmann, R. Ritch, and D. C. Hood, "Multifocal visual evoked potential responses in glaucoma patients with unilateral hemifield defects," *American journal of ophthalmology*, vol. 136, no. 1, pp. 34–40, 2003.

[55] S. Stiefelmeyer, A. S. Neubauer, T. Berninger, G. B. Arden, and G. Rudolph, "The multifocal pattern electroretinogram in glaucoma," *Vision research*, vol. 44, no. 1, pp. 103–112, 2004.

[56] P. H. Chu, H. H. Chan, and B. Brown, "Luminance-modulated adaptation of global flash mferg: fellow eye losses in asymmetric glaucoma," *Investigative ophthalmology & visual science*, vol. 48, no. 6, pp. 2626–2633, 2007.

[57] W.-c. Ho, O.-y. Wong, Y.-c. Chan, S.-w. Wong, C.-s. Kee, and H. H.-l. Chan, "Sign-dependent changes in retinal electrical activity with positive and negative defocus in the human eye," *Vision research*, vol. 52, no. 1, pp. 47–53, 2012.

[58] N. Hori, S. Komori, H. Yamada, A. Sawada, Y. Nomura, K. Mochizuki, and T. Yamamoto, "Assessment of macular function of glaucomatous eyes by multifocal electroretinograms," *Documenta Ophthalmologica*, vol. 125, no. 3, pp. 235–247, 2012.

[59] M. G. Todorova and A. M. Palmowski-Wolfe, "Mferg responses to long-duration white stimuli in glaucoma patients," *Documenta ophthalmologica*, vol. 122, no. 2, pp. 87–97, 2011.

[60] S. L. Graham, A. I. Klistorner, J. R. Grigg, and F. A. Billson, "Objective vep perimetry in glaucoma: asymmetry analysis to identify early deficits." *Journal of glaucoma*, vol. 9, no. 1, pp. 10–19, 2000.

[61] L. J. Frishman, S. Saszik, R. S. Harwerth, S. Viswanathan, Y. Li, E. L. Smith, J. G. Robson, G. Barnes *et al.*, "Effects of experimental glaucoma in macaques on the multifocal erg," *Documenta Ophthalmologica*, vol. 100, no. 2, pp. 231–251, 2000.

[62] E. A. Dale, D. C. Hood, V. C. Greenstein, and J. G. Odel, "A comparison of multifocal erg and frequency domain oct changes in patients with abnormalities of the retina," *Documenta ophthalmologica*, vol. 120, no. 2, pp. 175–186, 2010.

[63] R. Barraco, D. P. Adorno, M. Brai, and L. Tranchina, "A comparison among different techniques for human erg signals processing and classification," *Physica Medica*, vol. 30, no. 1, pp. 86–95, 2014.

[64] J. D. Forte, B. V. Bui, and A. J. Vingrys, "Wavelet analysis reveals dynamics of rat oscillatory potentials," *Journal of neuroscience methods*, vol. 169, no. 1, pp. 191–200, 2008.

[65] A. Consejo, T. Melcer, and J. J. Rozema, "Introduction to machine learning for ophthalmologists," in *Seminars in ophthalmology*, vol. 34, no. 1. Taylor & Francis, 2019, pp. 19–41.

[66] G. W. Armstrong and A. C. Lorch, "A (eye): a review of current applications of artificial intelligence and machine learning in ophthalmology," *International ophthalmology clinics*, vol. 60, no. 1, pp. 57–71, 2020.

[67] C. Bowd, R. N. Weinreb, M. Balasubramanian, I. Lee, G. Jang, S. Yousefi, L. M. Zangwill, F. A. Medeiros, C. A. Girkin, J. M. Liebmann *et al.*, "Glaucomatous

patterns in frequency doubling technology (fdt) perimetry data identified by unsupervised machine learning classifiers," *PloS one*, vol. 9, no. 1, p. e85941, 2014.

[68] S. Verma, M. E. Nongpiur, E. Atalay, X. Wei, R. Husain, D. Goh, S. A. Perera, and T. Aung, "Visual field progression in patients with primary angle-closure glaucoma using pointwise linear regression analysis," *Ophthalmology*, vol. 124, no. 7, pp. 1065–1071, 2017.

[69] E. Atalay, M. E. Nongpiur, S. C. Yap, T. T. Wong, D. Goh, R. Husain, S. A. Perera, and T. Aung, "Pattern of visual field loss in primary angle-closure glaucoma across different severity levels," *Ophthalmology*, vol. 123, no. 9, pp. 1957–1964, 2016.

[70] S. Yousefi, M. H. Goldbaum, E. S. Varnousfaderani, A. Belghith, T.-P. Jung, F. A. Medeiros, L. M. Zangwill, R. N. Weinreb, J. M. Liebmann, C. A. Girkin *et al.*, "Detecting glaucomatous change in visual fields: Analysis with an optimization framework," *Journal of biomedical informatics*, vol. 58, pp. 96–103, 2015.

[71] L. Boquete, J. M. Miguel-Jiménez, S. Ortega, J. Rodríguez-Ascariz, C. Pérez-Rico, and R. Blanco, "Multifocal electroretinogram diagnosis of glaucoma applying neural networks and structural pattern analysis," *Expert systems with applications*, vol. 39, no. 1, pp. 234–238, 2012.

[72] J. M. Miguel-Jiménez, R. Blanco, L. De-Santiago, A. Fernandez, J. M. Rodríguez-Ascariz, R. Barea, J. L. Martín-Sánchez, C. Amo, E. Sánchez-Morla, and L. Boquete, "Continuous-wavelet-transform analysis of the multifocal erg waveform in glaucoma

diagnosis," *Medical & biological engineering & computing*, vol. 53, no. 9, pp. 771–780, 2015.

[73] M. Sarossy, D. Kumar, and Z. Wu, "Relationship between glaucoma and complexity measures of the electroretinogram," in *2021 Seventh International conference on Bio Signals, Images, and Instrumentation (ICBSII)*. IEEE, 2021, pp. 1–4.

[74] Q. Li, C. Rajagopalan, and G. D. Clifford, "A machine learning approach to multi-level ecg signal quality classification," *Computer methods and programs in biomedicine*, vol. 117, no. 3, pp. 435–447, 2014.

[75] İ. S. Yapici, O. Erkaymaz, and R. U. Arslan, "A hybrid intelligent classifier to estimate obesity levels based on erg signals," *Physics Letters A*, vol. 399, p. 127281, 2021.

[76] B. Lei, G. Yao, K. Zhang, K. J. Hofeldt, and B. Chang, "Study of rod-and cone-driven oscillatory potentials in mice," *Investigative ophthalmology & visual science*, vol. 47, no. 6, pp. 2732–2738, 2006.

[77] H. A. Hancock and T. W. Kraft, "Oscillatory potential analysis and ergs of normal and diabetic rats," *Investigative ophthalmology & visual science*, vol. 45, no. 3, pp. 1002–1008, 2004.

[78] C.-J. Dong, P. Agey, and W. A. Hare, "Origins of the electroretinogram oscillatory potentials in the rabbit retina," *Visual neuroscience*, vol. 21, no. 4, pp. 533–543, 2004.

[79] S. M. Saszik, J. G. Robson, and L. J. Frishman, "The scotopic threshold response of the dark-adapted electroretinogram of the mouse," *The Journal of physiology*, vol. 543, no. 3, pp. 899–916, 2002.

[80] M. Marmor, A. Fulton, G. Holder, Y. Miyake, M. Brigell, and M. Bach, "Iscev standard for full-field clinical electroretinography (2008 update)," *Documenta Ophthalmologica*, vol. 118, no. 1, pp. 69–77, 2009.

[81] S. L. Grillo, C. L. Montgomery, H. M. Johnson, and P. Koulen, "Quantification of changes in visual function during disease development in a mouse model of pigmentary glaucoma," *Journal of glaucoma*, vol. 27, no. 9, p. 828, 2018.

[82] D. L. Demmin, Q. Davis, M. Roché, and S. M. Silverstein, "Electroretinographic anomalies in schizophrenia." *Journal of abnormal psychology*, vol. 127, no. 4, p. 417, 2018.

[83] M. Hébert, C. Mérette, A.-M. Gagné, T. Paccalet, I. Moreau, J. Lavoie, and M. Maziade, "The electroretinogram may differentiate schizophrenia from bipolar disorder," *Biological psychiatry*, vol. 87, no. 3, pp. 263–270, 2020.

[84] T. Lai, J. Ngai, R. Lai, and D. Lam, "Multifocal electroretinography changes in patients on ethambutol therapy," *Eye*, vol. 23, no. 8, pp. 1707–1713, 2009.

[85] T. Y. Lai, J. W. Ngai, W.-M. Chan, and D. S. Lam, "Visual field and multifocal electroretinography and their correlations in patients on hydroxychloroquine therapy," *Documenta ophthalmologica*, vol. 112, no. 3, pp. 177–187, 2006.

[86] M. Nebbioso, R. Grenga, and P. Karavitis, "Early detection of macular changes with multifocal erg in patients on antimalarial drug therapy," *Journal of ocular pharmacology and therapeutics*, vol. 25, no. 3, pp. 249–258, 2009.

[87] C. N. da Silva, L. F. N. Dourado, M. E. de Lima, and A. da Silva Cunha-Jr, "Pnpp-19 peptide as a novel drug candidate for topical glaucoma therapy through nitric oxide release," *Translational Vision Science & Technology*, vol. 9, no. 8, pp. 33–33, 2020.

[88] S. L. Grillo and P. Koulen, "Psychophysical testing in rodent models of glaucomatous optic neuropathy," *Experimental eye research*, vol. 141, pp. 154–163, 2015.

[89] S. J. McKinnon, C. L. Schlamp, and R. W. Nickells, "Mouse models of retinal ganglion cell death and glaucoma," *Experimental eye research*, vol. 88, no. 4, pp. 816–824, 2009.

[90] C. L. Montgomery, J. Keereetaweep, H. M. Johnson, S. L. Grillo, K. D. Chapman, and P. Koulen, "Changes in retinal n-acylethanolamines and their oxylipin derivatives during the development of visual impairment in a mouse model for glaucoma," *Lipids*, vol. 51, no. 7, pp. 857–866, 2016.

[91] S. L. Burroughs, S. Kaja, and P. Koulen, "Quantification of deficits in spatial visual function of mouse models for glaucoma," *Investigative ophthalmology & visual science*, vol. 52, no. 6, pp. 3654–3659, 2011.

[92] M. J. P. de Lara, C. Santano, A. Guzmán-Aránguez, F. J. Valiente-Soriano, M. Avilés-Trigueros, M. Vidal-Sanz, P. de la Villa, and J. Pintor, "Assessment of inner retina

dysfunction and progressive ganglion cell loss in a mouse model of glaucoma," *Experimental eye research*, vol. 122, pp. 40–49, 2014.

[93] S. Kaja, Y. Naumchuk, S. L. Grillo, P. K. Borden, and P. Koulen, "Differential up-regulation of vesl-1/homer 1 protein isoforms associated with decline in visual performance in a preclinical glaucoma model," *Vision research*, vol. 94, pp. 16–23, 2014.

[94] S. L. Grillo, J. Keereetaweep, M. A. Grillo, K. D. Chapman, and P. Koulen, "N-palmitoylethanolamine depot injection increased its tissue levels and those of other acylethanolamide lipids," *Drug design, development and therapy*, vol. 7, p. 747, 2013.

[95] S. H. Jambukia, V. K. Dabhi, and H. B. Prajapati, "Classification of ecg signals using machine learning techniques: A survey," in *2015 International Conference on Advances in Computer Engineering and Applications*. IEEE, 2015, pp. 714–721.

[96] S. Khalid, T. Khalil, and S. Nasreen, "A survey of feature selection and feature extraction techniques in machine learning," in *2014 science and information conference*. IEEE, 2014, pp. 372–378.

[97] J. W. Graham, P. E. Cumsille, and A. E. Shevock, "Methods for handling missing data." 2013.

[98] H. Aguinis, R. K. Gottfredson, and H. Joo, "Best-practice recommendations for defining, identifying, and handling outliers," *Organizational Research Methods*, vol. 16, no. 2, pp. 270–301, 2013.

[99] X. Wan, "Influence of feature scaling on convergence of gradient iterative algorithm," in *Journal of Physics: Conference Series*, vol. 1213, no. 3. IOP Publishing, 2019, p. 032021.

[100] D. W. Aha and R. L. Bankert, "A comparative evaluation of sequential feature selection algorithms," in *Learning from data*. Springer, 1996, pp. 199–206.

[101] I. Guyon, S. Gunn, M. Nikravesh, and L. A. Zadeh, *Feature extraction: foundations and applications*. Springer, 2008, vol. 207.

[102] A. Asgharzadeh-Bonab, M. C. Amirani, and A. Mehri, "Spectral entropy and deep convolutional neural network for ecg beat classification," *Biocybernetics and Biomedical Engineering*, vol. 40, no. 2, pp. 691–700, 2020.

[103] R. J. Martis, C. Chakraborty, and A. K. Ray, "Wavelet-based machine learning techniques for ecg signal analysis," in *Machine learning in healthcare informatics*. Springer, 2014, pp. 25–45.

[104] I. Daubechies, "Cbms-nsf regional conference series in applied mathematics," *Ten lectures on wavelets*, vol. 61, 1992.

[105] Q. Zhao and L. Zhang, "Ecg feature extraction and classification using wavelet transform and support vector machines," in *2005 International Conference on Neural Networks and Brain*, vol. 2. IEEE, 2005, pp. 1089–1092.

[106] A. Neumaier and T. Schneider, "Estimation of parameters and eigenmodes of multivariate autoregressive models," *ACM Transactions on Mathematical Software (TOMS)*, vol. 27, no. 1, pp. 27–57, 2001.

[107] T. Li and M. Zhou, "Ecg classification using wavelet packet entropy and random forests," *Entropy*, vol. 18, no. 8, p. 285, 2016.

[108] R. F. Leonarduzzi, G. Schlotthauer, and M. E. Torres, "Wavelet leader based multifractal analysis of heart rate variability during myocardial ischaemia," in *2010 Annual International Conference of the IEEE Engineering in Medicine and Biology*. IEEE, 2010, pp. 110–113.

[109] E. A. Maharaj and A. M. Alonso, "Discriminant analysis of multivariate time series: Application to diagnosis based on ecg signals," *Computational Statistics & Data Analysis*, vol. 70, pp. 67–87, 2014.

[110] Y. Saeys, I. Inza, and P. Larranaga, "A review of feature selection techniques in bioinformatics," *bioinformatics*, vol. 23, no. 19, pp. 2507–2517, 2007.

[111] C. Ding and H. Peng, "Minimum redundancy feature selection from microarray gene expression data," *Journal of bioinformatics and computational biology*, vol. 3, no. 02, pp. 185–205, 2005.

[112] G. A. Darbellay and I. Vajda, "Estimation of the information by an adaptive partitioning of the observation space," *IEEE Transactions on Information Theory*, vol. 45, no. 4, pp. 1315–1321, 1999.

[113] Z. Zhao, R. Anand, and M. Wang, "Maximum relevance and minimum redundancy feature selection methods for a marketing machine learning platform," in *2019 IEEE International Conference on Data Science and Advanced Analytics (DSAA)*. IEEE, 2019, pp. 442–452.

[114] D. Bzdok, N. Altman, and M. Krzywinski, "Points of significance: statistics versus machine learning," *Nature Methods 2018a*, pp. 1–7, 2018.

[115] A. Navada, A. N. Ansari, S. Patil, and B. A. Sonkamble, "Overview of use of decision tree algorithms in machine learning," in *2011 IEEE control and system graduate research colloquium*. IEEE, 2011, pp. 37–42.

[116] G. C. Cawley and N. L. Talbot, "Efficient leave-one-out cross-validation of kernel fisher discriminant classifiers," *Pattern Recognition*, vol. 36, no. 11, pp. 2585–2592, 2003.

[117] W. S. Noble, "What is a support vector machine?" *Nature biotechnology*, vol. 24, no. 12, pp. 1565–1567, 2006.

[118] M.-L. Zhang and Z.-H. Zhou, "Ml-knn: A lazy learning approach to multi-label learning," *Pattern recognition*, vol. 40, no. 7, pp. 2038–2048, 2007.

[119] T. G. Dietterich, "Ensemble methods in machine learning," in *International workshop on multiple classifier systems*. Springer, 2000, pp. 1–15.

[120] M. J. P. de Lara, A. Guzmán-Aránguez, P. de la Villa, J. I. Díaz-Hernández, M. T. Miras-Portugal, and J. Pintor, "Increased levels of extracellular atp in glaucomatous retinas: possible role of the vesicular nucleotide transporter during the development of the pathology," *Molecular vision*, vol. 21, p. 1060, 2015.

[121] V. Porciatti, "Electrophysiological assessment of retinal ganglion cell function," *Experimental eye research*, vol. 141, pp. 164–170, 2015.

[122] C. W. Tyler, "Specific deficits of flicker sensitivity in glaucoma and ocular hypertension." *Investigative ophthalmology & visual science*, vol. 20, no. 2, pp. 204–212, 1981.

[123] L. J. Wilsey and B. Fortune, "Electroretinography in glaucoma diagnosis," *Current opinion in ophthalmology*, vol. 27, no. 2, p. 118, 2016.

[124] A. Hermas, "Sensitivity and specificity of the uniform field erg in glaucoma detection," Ph.D. dissertation, Université d'Ottawa/University of Ottawa, 2019.

[125] G. Beykin, A. M. Norcia, V. J. Srinivasan, A. Dubra, and J. L. Goldberg, "Discovery and clinical translation of novel glaucoma biomarkers," *Progress in Retinal and eye Research*, vol. 80, p. 100875, 2021.

[126] H. Seo, M. Badiei Khuzani, V. Vasudevan, C. Huang, H. Ren, R. Xiao, X. Jia, and L. Xing, "Machine learning techniques for biomedical image segmentation: An

overview of technical aspects and introduction to state-of-art applications," *Medical physics*, vol. 47, no. 5, pp. e148–e167, 2020.

[127] Y. Zhang and C. Ling, "A strategy to apply machine learning to small datasets in materials science," *Npj Computational Materials*, vol. 4, no. 1, pp. 1–8, 2018.

[128] S. Yadav and S. Shukla, "Analysis of k-fold cross-validation over hold-out validation on colossal datasets for quality classification," in *2016 IEEE 6th International conference on advanced computing (IACC)*. IEEE, 2016, pp. 78–83.

[129] K. Duan, S. S. Keerthi, and A. N. Poo, "Evaluation of simple performance measures for tuning svm hyperparameters," *Neurocomputing*, vol. 51, pp. 41–59, 2003.

[130] S. Varma and R. Simon, "Bias in error estimation when using cross-validation for model selection," *BMC bioinformatics*, vol. 7, no. 1, pp. 1–8, 2006.

[131] M. Feurer and F. Hutter, "Hyperparameter optimization," in *Automated machine learning*. Springer, Cham, 2019, pp. 3–33.

[132] M. Kuhn and K. Johnson, "Measuring predictor importance," in *Applied predictive modeling*. Springer, 2013, pp. 463–485.

[133] B. Lachenmayr and S. Drance, "The selective effects of elevated intraocular pressure on temporal resolution." *German journal of ophthalmology*, vol. 1, no. 1, pp. 26–31, 1992.

[134] F. K. Horn, J. B. Jonas, M. Korth, A. JÜNEMANN, and A. GRÜNDLER, "The full-field flicker test in early diagnosis of chronic open-angle glaucoma," *American journal of ophthalmology*, vol. 123, no. 3, pp. 313–319, 1997.

[135] K. K. Yoshiyama and C. A. Johnson, "Which method of flicker perimetry is most effective for detection of glaucomatous visual field loss?" *Investigative ophthalmology & visual science*, vol. 38, no. 11, pp. 2270–2277, 1997.

[136] I. F. S. A. Kabir, F. Safiyullah, E. Y. K. Ng, and V. W. Tam, "New analytical wake models based on artificial intelligence and rivalling the benchmark full-rotor cfd predictions under both uniform and abl inflows," *Energy*, vol. 193, p. 116761, 2020.

[137] S. Liu and I. Janajreh, "Development and application of an improved blade element momentum method model on horizontal axis wind turbines," *International Journal of Energy and Environmental Engineering*, vol. 3, no. 1, pp. 1–10, 2012.

[138] Z. Sun, J. Chen, W. Z. Shen, and W. J. Zhu, "Improved blade element momentum theory for wind turbine aerodynamic computations," *Renewable energy*, vol. 96, pp. 824–831, 2016.

[139] I. F. S. A. Kabir and E. Y. K. Ng, "Insight into stall delay and computation of 3d sectional aerofoil characteristics of nrel phase vi wind turbine using inverse bem and improvement in bem analysis accounting for stall delay effect," *Energy*, vol. 120, pp. 518–536, 2017.

[140] I. Herráez, B. Stoevesandt, and J. Peinke, "Insight into rotational effects on a wind turbine blade using navier–stokes computations," *Energies*, vol. 7, no. 10, pp. 6798–6822, 2014.

[141] B. Plaza, R. Bardera, and S. Visiedo, "Comparison of bem and cfd results for mexico rotor aerodynamics," *Journal of Wind Engineering and Industrial Aerodynamics*, vol. 145, pp. 115–122, 2015.

[142] J. F. Manwell, J. G. McGowan, and A. L. Rogers, *Wind energy explained: theory, design and application*. John Wiley & Sons, 2010.

[143] T. Burton, N. Jenkins, D. Sharpe, and E. Bossanyi, *Wind energy handbook*. John Wiley & Sons, 2011.

[144] C. Lindenburg, "Investigation into rotor blade aerodynamics," *Energy research Centre of the Netherlands (ECN) Wind Energy publication, ECN-C–03-025*, 2003.

[145] D. Hu, O. Hua, and Z. Du, "A study on stall-delay for horizontal axis wind turbine," *Renewable Energy*, vol. 31, no. 6, pp. 821–836, 2006.

[146] S.-P. Breton, F. N. Coton, and G. Moe, "A study on rotational effects and different stall delay models using a prescribed wake vortex scheme and nrel phase vi experiment data," *Wind Energy: An International Journal for Progress and Applications in Wind Power Conversion Technology*, vol. 11, no. 5, pp. 459–482, 2008.

[147] S.-P. Breton, "Study of the stall delay phenomenon and of wind turbine blade dynamics using numerical approaches and nrelâs wind tunnel tests," 2008.

[148] M. Elgammi and T. Sant, "A new stall delay algorithm for predicting the aerodynamics loads on wind turbine blades for axial and yawed conditions," *Wind Energy*, vol. 20, no. 9, pp. 1645–1663, 2017.

[149] S. Schreck and M. Robinson, "Rotational augmentation of horizontal axis wind turbine blade aerodynamic response," *Wind Energy: An International Journal for Progress and Applications in Wind Power Conversion Technology*, vol. 5, no. 2-3, pp. 133–150, 2002.

[150] S. Guntur, C. Bak, and N. N. Sørensen, "Analysis of 3d stall models for wind turbine blades using data from the mexico experiment," in *13th International Conference on Wind Engineering*, 2012.

[151] H. Himmelskamp, *Profile investigations on a rotating airscrew*. Ministry of Aircraft Production, 1947.

[152] W. Banks and G. Gadd, "Delaying effect of rotation on laminar separation," *AIAA journal*, vol. 1, no. 4, pp. 941–941, 1963.

[153] H. Dwyer and W. McCROSKE, "Crossflow and unsteady boundary-layer effects on rotating blades," *AIAA Journal*, vol. 9, no. 8, pp. 1498–1505, 1971.

[154] D. Milborrow, "Changes in aerofoil characteristics due to radial flow on rotating blades," in *Proceedings of the 7-th BWEA conference*, 1985.

[155] H. A. Madsen and H. Christensen, "On the relative importance of rotational, unsteady and three-dimensional effects on the hawt rotor aerodynamics," *Wind Engineering*, pp. 405–415, 1990.

[156] D. Wood, "A three-dimensional analysis of stall-delay on a horizontal-axis wind turbine," *Journal of wind engineering and Industrial aerodynamics*, vol. 37, no. 1, pp. 1–14, 1991.

[157] J. Narramore and R. Vermeland, "Navier-stokes calculations of inboard stall delay due to rotation," *Journal of aircraft*, vol. 29, no. 1, pp. 73–78, 1992.

[158] H. Snel, R. Houwink, and J. Bosschers, "Sectional prediction of lift coefficients on rotating wind turbine blades in stall," 1994.

[159] D. Simms, S. Schreck, M. Hand, and L. J. Fingersh, "Nrel unsteady aerodynamics experiment in the nasa-ames wind tunnel: a comparison of predictions to measurements," National Renewable Energy Lab., Golden, CO (US), Tech. Rep., 2001.

[160] S. Guntur and N. N. Sørensen, "An evaluation of several methods of determining the local angle of attack on wind turbine blades," in *Journal of Physics: Conference Series*, vol. 555, no. 1. IOP Publishing, 2014, p. 012045.

[161] I. F. S. A. Kabir, "Improvement of bem analysis to incorporate stall delay effect and the study of atmospheric boundary layer effect on the wake characteristics of nrel phase vi turbine," Ph.D. dissertation, School of Mechanical and Aerospace Engineering, Nanyang Technological University, Singapore, 2018.

[162] A. Betz, "Das maximum der theoretisch möglichen ausnutzung des windes durch windmotoren," *Zeitschrift fur das gesamte Turbinenwesten*, vol. 20, 1920.

[163] H. Glauert, *The elements of aerofoil and airscrew theory*. Cambridge university press, 1983.

[164] M. Hansen, "Aerodynamics of wind turbinessecond edition earthscan," *London, UK*, 2008.

[165] A. Hansen and C. Butterfield, "Aerodynamics of horizontal-axis wind turbines," *Annual Review of Fluid Mechanics*, vol. 25, no. 1, pp. 115–149, 1993.

[166] J. G. Leishman, "Challenges in modelling the unsteady aerodynamics of wind turbines," *Wind Energy: An International Journal for Progress and Applications in Wind Power Conversion Technology*, vol. 5, no. 2-3, pp. 85–132, 2002.

[167] H. Rahimi, J. Schepers, W. Z. Shen, N. R. García, M. Schneider, D. Micallef, C. S. Ferreira, E. Jost, L. Klein, and I. Herráez, "Evaluation of different methods for determining the angle of attack on wind turbine blades with cfd results under axial inflow conditions," *Renewable Energy*, vol. 125, pp. 866–876, 2018.

[168] H. Snel, R. Houwink, J. Bosschers, W. Piers, G. J. Van Bussel, and A. Bruining, "Sectional prediction of sd effects for stalled flow on rotating blades and comparison with measurements," 1993.

[169] P. Chaviaropoulos and M. O. Hansen, "Investigating three-dimensional and rotational effects on wind turbine blades by means of a quasi-3d navier-stokes solver," *J. Fluids Eng.*, vol. 122, no. 2, pp. 330–336, 2000.

[170] N. V. Raj, "An improved semi-empirical model for 3-d post-stall effects in horizontal axis wind turbines," Ph.D. dissertation, University of Illinois at Urbana-Champaign, 2000.

[171] J. J. Corrigan and J. Schillings, "Empirical model for stall delay due to rotation," in *American Helicopter Society Aeromechanics Specialists Conference*, 1994, pp. 1–16.

[172] C. Bak, J. Johansen, and P. B. Andersen, "Three-dimensional corrections of airfoil characteristics based on pressure distributions," in *Proceedings of the European Wind Energy Conference*, 2006, pp. 1–10.

[173] Z. Du and M. Selig, "A 3-d stall-delay model for horizontal axis wind turbine performance prediction," in *1998 ASME Wind Energy Symposium*, 1998, p. 21.

[174] H. Dumitrescu, V. Cardoş, and A. Dumitrache, "Modelling of inboard stall delay due to rotation," in *Journal of Physics: Conference Series*, vol. 75, no. 1. IOP Publishing, 2007, p. 012022.

[175] H. Dumitrescu and V. Cardoş, "Inboard boundary layer state on wind turbine blades," *ZAMM-Journal of Applied Mathematics and Mechanics/Zeitschrift für Angewandte*

Mathematik und Mechanik: Applied Mathematics and Mechanics, vol. 89, no. 3, pp. 163–173, 2009.

[176] H. Dumitrescu and V. Cardos, "Inboard stall delay due to rotation," *Journal of aircraft*, vol. 49, no. 1, pp. 101–107, 2012.

[177] M. N. Hamlaoui, A. Smaili, and H. Fellouah, "Improved bem method for hawt performance predictions," in *2018 International Conference on Wind Energy and Applications in Algeria (ICWEAA)*. IEEE, 2018, pp. 1–6.

[178] M. Hand, D. Simms, L. Fingersh, D. Jager, J. Cotrell, S. Schreck, and S. Larwood, "Unsteady aerodynamics experiment phase vi: wind tunnel test configurations and available data campaigns," National Renewable Energy Lab., Golden, CO.(US), Tech. Rep., 2001.

[179] J. Schepers, T. Lutz, K. Boorsma, S. Gomez-Iradi, I. Herraez, L. Oggiano, H. Rahimi, P. Schaffarczyk, G. Pirrung, H. A. Madsen *et al.*, "Final report of iea wind task 29 mexnext (phase 3)," 2018.

[180] S. Purohit, I. F. S. A. Kabir, and E. Y. K. Ng, "On the accuracy of urans and les-based cfd modeling approaches for rotor and wake aerodynamics of the (new) mexico wind turbine rotor phase-iii," *Energies*, vol. 14, no. 16, p. 5198, 2021.

[181] M. K. Gajendran, M. Z. Khan, and M. A. K. Khattak, "Ecg classification using deep transfer learning," in *2021 4th International Conference on Information and Computer Technologies (ICICT)*. IEEE, 2021, pp. 1–5.

[182] V. Jahmunah, E. Ng, T. R. San, and U. R. Acharya, "Automated detection of coronary artery disease, myocardial infarction and congestive heart failure using gaborcnn model with ecg signals," *Computers in biology and medicine*, vol. 134, p. 104457, 2021.

[183] M. K. Gajendran, L. J. Rohowetz, P. Koulen, and A. Mehdizadeh, "Novel machine-learning based framework using electroretinography data for the detection of early-stage glaucoma," *Frontiers in Neuroscience*, vol. 15, 2022.

[184] F. Karray, F. O. Karray, and C. W. De Silva, *Soft computing and intelligent systems design: theory, tools, and applications*. Pearson Education, 2004.

[185] S. N. Londhe and P. R. Dixit, "Genetic programming: a novel computing approach in modeling water flows," in *Genetic programming-New approaches and successful applications*. IntechOpen Publishing, 2012.

[186] R. R. Yager, L. A. Zadeh, B. Kosko, and S. Grossberg, "Fuzzy sets, neural networks, and soft computing," Tech. Rep., 1994.

[187] L. Magdalena, "What is soft computing? revisiting possible answers," *International Journal of Computational Intelligence Systems*, vol. 3, no. 2, pp. 148–159, 2010.

[188] D. Ibrahim, "An overview of soft computing," *Procedia Computer Science*, vol. 102, pp. 34–38, 2016.

[189] F. Safiyullah, S. Sulaiman, M. Naz, M. Jasmani, and S. Ghazali, "Prediction on performance degradation and maintenance of centrifugal gas compressors using genetic programming," *Energy*, vol. 158, pp. 485–494, 2018.

[190] N. R. Draper and H. Smith, *Applied regression analysis*. John Wiley & Sons, 1998, vol. 326.

[191] S. Chatterjee and A. S. Hadi, *Regression analysis by example*. John Wiley & Sons, 2015.

[192] G. F. Smits and M. Kotanchek, "Pareto-front exploitation in symbolic regression," in *Genetic programming theory and practice II*. Springer, 2005, pp. 283–299.

[193] C. O. Morales and K. R. Vázquez, "Symbolic regression problems by genetic programming with multi-branches," in *Mexican International Conference on Artificial Intelligence*. Springer, 2004, pp. 717–726.

[194] E. Stinstra, G. Rennen, and G. Teeuwen, "Metamodeling by symbolic regression and pareto simulated annealing," *Structural and Multidisciplinary Optimization*, vol. 35, no. 4, pp. 315–326, 2008.

[195] M. Schmidt and H. Lipson, "Distilling free-form natural laws from experimental data," *science*, vol. 324, no. 5923, pp. 81–85, 2009.

[196] S. Kirkpatrick, C. D. Gelatt, and M. P. Vecchi, "Optimization by simulated annealing," *science*, vol. 220, no. 4598, pp. 671–680, 1983.

[197] M. K. Gajendran, I. F. S. A. Kabir, S. Purohit, and E. Ng, "On the limitations of machine learning (ml) methodologies in predicting the wake characteristics of wind turbines," in *Renewable Energy Systems in Smart Grid*. Springer, 2022, pp. 15–23.

[198] N. N. Sørensen, J. Michelsen, and S. Schreck, "Navier–stokes predictions of the nrel phase vi rotor in the nasa ames 80 ft× 120 ft wind tunnel," *Wind Energy: An International Journal for Progress and Applications in Wind Power Conversion Technology*, vol. 5, no. 2-3, pp. 151–169, 2002.

[199] J. Johansen and N. N. Sørensen, "Aerofoil characteristics from 3d cfd rotor computations," *Wind Energy: An International Journal for Progress and Applications in Wind Power Conversion Technology*, vol. 7, no. 4, pp. 283–294, 2004.

[200] J. Tangler and D. Kocurek, "Wind turbine post-stall airfoil performance characteristics guidelines for blade-element momentum methods," in *43rd AIAA Aerospace Sciences Meeting and Exhibit*, 2005, p. 591.

[201] T. Sant, G. van Kuik, and G. Van Bussel, "Estimating the angle of attack from blade pressure measurements on the nrel phase vi rotor using a free wake vortex model: axial conditions," *Wind Energy: An International Journal for Progress and Applications in Wind Power Conversion Technology*, vol. 9, no. 6, pp. 549–577, 2006.

[202] J. Schepers and R. Van Rooij, "Analysis of aerodynamic measurements on a model wind turbine placed in the nasa-ames tunnel. contribution of ecn and tud to iea wind task xx," 2008.

[203] L. A. Viterna and R. D. Corrigan, "Fixed pitch rotor performance of large horizontal axis wind turbines," in *NASA Lewis Research Center: Energy Production and Conversion Workshop, Cleveland, OH, United States January*, vol. 1, 1982.

[204] Z. Du and M. Selig, "The effect of rotation on the boundary layer of a wind turbine blade," *Renewable Energy*, vol. 20, no. 2, pp. 167–181, 2000.

[205] I. F. S. A. Kabir and E. Y. K. Ng, "Effect of different atmospheric boundary layers on the wake characteristics of nrel phase vi wind turbine," *Renewable energy*, vol. 130, pp. 1185–1197, 2019.

[206] S. Purohit, I. F. S. A. Kabir, and E. Y. K. Ng, "Evaluation of three potential machine learning algorithms for predicting the velocity and turbulence intensity of a wind turbine wake," *Renewable Energy*, vol. 184, pp. 405–420, 2022.

[207] P. J. Moriarty and A. C. Hansen, "Aerodyn theory manual," National Renewable Energy Lab., Golden, CO (US), Tech. Rep., 2005.

[208] G. Bangga, T. Lutz, and M. Arnold, "An improved second-order dynamic stall model for wind turbine airfoils," *Wind Energy Science*, vol. 5, no. 3, pp. 1037–1058, 2020.

[209] J.-P. Küppers and T. Reinicke, "A wavenet-based fully stochastic dynamic stall model," *Wind Energy Science Discussions*, pp. 1–24, 2022.

[210] C. Ferreira, W. Yu, A. Sala, and A. Viré, "Dynamic inflow model for a floating horizontal axis wind turbine in surge motion," *Wind Energy Science*, vol. 7, no. 2, pp. 469–485, 2022.

[211] F. Castellani, D. Astolfi, F. Natili, and F. Mari, "The yawing behavior of horizontal-axis wind turbines: a numerical and experimental analysis," *Machines*, vol. 7, no. 1, p. 15, 2019.

[212] G. Kavari, M. Tahani, and M. Mirhosseini, "Wind shear effect on aerodynamic performance and energy production of horizontal axis wind turbines with developing blade element momentum theory," *Journal of Cleaner Production*, vol. 219, pp. 368–376, 2019.

VITA

Mohan Kumar Gajendran is currently pursuing a Ph.D. degree in mechanical engineering and mathematics at University of Missouri Kansas City (UMKC). He was a Guest Researcher with the Delft University of Technology, The Netherlands, in 2017. His research interests include computational fluid dynamics, signal processing, turbulence modeling, machine learning, and deep learning.